Stepwise activation mechanism of the scramblase nhTMEM16 revealed by cryo-EM

Valeria Kalienkova[1], Vanessa Clerico Mosina[2], Laura Bryner[1], Gert T. Oostergetel[2], Raimund Dutzler[1*] and Cristina Paulino[2*]

[1]Department of Biochemistry, University of Zürich, Winterthurer Str. 190, CH-8057 Zürich, Switzerland

[2]Department of Structural Biology at the Groningen Biomolecular Sciences and Biotechnology Institute, University of Groningen, Nijenborgh 7, 9747 AG Groningen, The Netherlands

[*]For correspondence: dutzler@bioc.uzh.ch (R.D.), c.paulino@rug.nl (C.P.)

Abstract

Scramblases catalyze the movement of lipids between both leaflets of a bilayer. Whereas the X-ray structure of the protein nhTMEM16 has previously revealed the architecture of a Ca^{2+}-dependent lipid scramblase, its regulation mechanism has remained elusive. Here, we have used cryo-electron microscopy and functional assays to address this question. Ca^{2+}-bound and Ca^{2+}-free conformations of nhTMEM16 in detergent and lipid nanodiscs illustrate the interactions with its environment and they reveal the conformational changes underlying its activation. In this process, Ca^{2+}-binding induces a stepwise transition of the catalytic subunit cavity, converting a closed cavity that is shielded from the membrane in the absence of ligand, into a polar furrow that becomes accessible to lipid headgroups in the Ca^{2+}-bound state. Additionally, our structures demonstrate how nhTMEM16 distorts the membrane at both entrances of the subunit cavity, thereby decreasing the energy barrier for lipid movement.

Impact statement: cryo-EM reveals the properties of distinct conformations occupied during activation of the lipid scramblase nhTMEM16 and provides new insights into its interactions with the lipid environment.

Introduction

The movement of lipids between both leaflets of a phospholipid bilayer, which is also referred to as lipid flip-flop, is energetically unfavorable since it requires the transfer of the polar headgroup from its aqueous environment across the hydrophobic core of the membrane (Kornberg and McConnell, 1971). Consequently, spontaneous lipid flip-flop is rare and occurs at a time scale of several hours. Whereas the sparsity of this event permits the maintenance of lipid asymmetry, there are processes that require the rapid transbilayer movement of lipids (Bevers and Williamson, 2016; Sanyal and Menon, 2009). Proteins that facilitate this movement by lowering the associated high energy barrier are termed lipid scramblases (Pomorski and Menon, 2006; Williamson, 2015). Lipid scramblases are generally non-selective and do not require the input of energy. They participate in various cellular functions ranging from lipid signaling during blood coagulation and apoptosis to the synthesis of membranes, cell division and exocytosis (Nagata et al., 2016; Whitlock and Hartzell, 2016). First structural insight into lipid scrambling was provided from the X-ray structure of the fungal protein from *Nectria haematococca*, termed nhTMEM16 (Brunner et al., 2014). This protein is part of the TMEM16 family (Milenkovic et al., 2010), which encompasses calcium-activated ion channels and lipid scramblases with a conserved molecular architecture (Brunner et al., 2016; Caputo et al., 2008; Falzone et al., 2018; Schroeder et al., 2008; Suzuki et al., 2013; Suzuki et al., 2010; Yang et al., 2008). As common for the family, nhTMEM16 is a homodimer with subunits containing a cytoplasmic domain and a transmembrane unit composed of 10 membrane-spanning segments. The lipid permeation path is defined by a structural entity termed the 'subunit cavity', which is located at the periphery of each subunit. In the X-ray structure, which was obtained in the presence of Ca^{2+}, this site exposes a continuous polar cavity that spans the entire membrane and that is of appropriate size to harbor a lipid headgroup (Brunner et al., 2014).

51 The 'subunit cavity' is believed to provide a pathway for the polar moieties of lipids across the
52 membrane, whereas the apolar acyl chains remain embedded in the hydrophobic core of the
53 membrane (Bethel and Grabe, 2016; Brunner et al., 2014; Jiang et al., 2017; Lee et al., 2018;
54 Malvezzi et al., 2018; Stansfeld et al., 2015). This process resembles a credit-card mechanism for
55 lipid scrambling, which was previously proposed based on theoretical considerations (Pomorski
56 and Menon, 2006). Although in this structure, Ca^{2+} ions were identified to bind to a conserved site
57 in the transmembrane domain, the mechanism of how Ca^{2+} activates the protein and how the
58 protein interacts with the surrounding lipids remained elusive. To gain insight into these questions,
59 we have determined structures of the protein in Ca^{2+}-bound and Ca^{2+}-free conformations by single
60 particle cryo-electron microscopy (cryo-EM), both in detergent and in a membrane environment
61 and we have characterized the effect of mutants on the activation process. Our data reveal two
62 essential features of the protein. They show how the protein deforms the membrane to lower the
63 energy barrier for lipid movement and to steer translocating lipids towards the subunit cavity.
64 Additionally, they define the conformational changes leading to the opening of the subunit cavity,
65 which is shielded from the membrane in a Ca^{2+}-free conformation, but exposes a hydrophilic
66 furrow for the permeation of lipids upon Ca^{2+} binding in a stepwise process involving coupled
67 ligand-dependent and ligand-independent steps.

68

69 **Results**

70 **Structural characterization of nhTMEM16 in detergent**

71 For our investigations of the ligand-induced activation mechanism of the lipid scramblase
72 nhTMEM16, we have recombinantly expressed the protein in the yeast *S. cerevisiae*, purified it in
73 the detergent n-Dodecyl β-D-maltoside (DDM) in the absence of Ca^{2+} and added Ca^{2+} during

74 sample preparation for structure determination and transport experiments. We have reconstituted
75 the purified protein into liposomes of different composition containing fluorescently labeled lipids
76 and characterized lipid transport using an assay that follows the irreversible decay of the
77 fluorescence upon addition of the membrane-impermeable reducing agent dithionite to the outside
78 of the liposomes (Brunner et al., 2014; Malvezzi et al., 2013; Ploier and Menon, 2016). In these
79 experiments we find a Ca^{2+}-dependent increase of transport but also a pronounced basal activity
80 of the protein in absence of Ca^{2+}, which was previously described as a hallmark of fungal
81 TMEM16 scramblases (Brunner et al., 2014; Malvezzi et al., 2013) (Figure 1-figure supplement
82 1). For the structural characterization of nhTMEM16, we have initially studied Ca^{2+}-bound and
83 Ca^{2+}-free samples in detergent by cryo-EM. By this approach, we have obtained two datasets of
84 high quality and of sufficient resolution (*i.e.* 3.6 Å for Ca^{2+}-bound and 3.7 Å for Ca^{2+}-free
85 conditions) for a detailed interpretation by an atomic model (Figure 1; Figure 1-figure supplements
86 2-4; Table 1). In the structure determined in the presence of Ca^{2+}, we find a conformation of the
87 protein, which closely resembles the X-ray structure with a root mean square deviation (RMSD)
88 of Cα atoms of 0.66 Å between the two structures (Figure 1D,E). The high similarity prevails
89 irrespective of the absence of crystal packing interactions and despite of the fact that the sample
90 used for cryo-EM was only briefly exposed to Ca^{2+} at a comparably low (*i.e.* 300 μM)
91 concentration, whereas for the X-ray structure, the protein was exposed to Ca^{2+} during purification
92 and crystallization at a 10-fold higher concentration (Brunner et al., 2014). Cryo-EM density at
93 the conserved Ca^{2+}-binding site, contained within each subunit of the homodimer, clearly indicates
94 the presence of two bound Ca^{2+} ions located at the position originally identified in the X-ray
95 structure (Figure 1F) (Brunner et al., 2014). Remarkably, we found a very similar structure of the
96 protein in the absence of Ca^{2+}, thus underlining the stability of this conformation in detergent

97 solution (Figure 1G,H). Although both datasets display equivalent conformations of the protein,
98 the structure determined in the absence of Ca^{2+} clearly shows an altered distribution of the divalent
99 ligand in its binding site, concomitant with a weaker density of the C-terminal part of α6 indicating
100 its increased mobility (Figure 1G,I; Figure1-figure supplement 3). The same region was previously
101 identified as key structural element in the Ca^{2+}-regulation of TMEM16A (Dang et al., 2017;
102 Paulino et al., 2017a; Peters et al., 2018). In the cryo-EM density, both strong peaks of the ligand
103 found in the Ca^{2+}-bound conformation are absent and instead replaced by weak residual density at
104 low contour located at the position of the lower Ca^{2+} ion (Figure 1F,I). Due to the presence of
105 millimolar amounts of EGTA in the buffer, the resulting free Ca^{2+}-concentration is in the pM
106 range, well below the estimated nM potency of the divalent cation (Figure 1-figure supplement 1).
107 Thus, whereas we do not want to exclude the possibility of Ca^{2+} binding at low occupancy, this
108 density might as well correspond to a bound Na^{+} ion, which is present in the sample buffer at a
109 concentration of 150 mM (*i.e.* at a 10^{10} times higher concentration compared to Ca^{2+}). We think
110 that the stability of the open conformation displayed in the structures of the protein in detergent,
111 irrespectively of the presence of bound Ca^{2+}, does not reflect an intrinsic rigidity of the subunit
112 cavity. Instead, it is likely a consequence of experimental conditions, which stabilize the observed
113 conformation of the protein. This is in accordance with residual density from the headgroup of a
114 bound detergent molecule at the upper part of the lipid translocation path found in both datasets,
115 which might prevent subunit cavity closure (Figure 1-figure supplement 5). Interestingly, the
116 detergent molecule is interacting with Tyr 439, a residue that was shown to be essential for lipid
117 translocation in MD simulations and functional studies (Lee et al., 2018). The Ca^{2+}-free structure
118 in detergent thus likely displays a conformation that is responsible for the basal activity observed

119 for nhTMEM16 and other fungal scramblases (Figure 1-figure supplement 1) (Brunner et al., 2014;
120 Malvezzi et al., 2013). We expect this state to be less populated in a lipid bilayer.
121
122 **Structure of the Ca^{2+}-free state of nhTMEM16 in lipid nanodiscs**
123 The absence of conformational changes in the subunit cavity of nhTMEM16 in detergents
124 motivated us to study the structure of the protein in a lipid bilayer. For that purpose, we have
125 reconstituted nhTMEM16 into nanodiscs of different sizes using a lipid composition at which the
126 protein retains its lipid scrambling activity, although with considerably slower kinetics (Figure 1-
127 figure supplement 1C). In order to make sure that the scramblase is surrounded by a sufficiently
128 large membrane area, we assembled 2N2 scaffolding proteins with nhTMEM16 at three different
129 lipid to protein ratios (LPR) in the absence of Ca^{2+} and collected small datasets for all of them
130 (Figure 2-figure supplement 1). In all cases, the protein is located close to the center of an elliptic
131 disc with its long dimension oriented about parallel to the shortest side of the disc, a behavior that
132 is more pronounced in larger discs obtained at high lipid to protein ratios (Figure 2-figure
133 supplement 1). The orientation reflects a preference of lipids for locations distant from the subunit
134 cavity, which appears to deform the nanodisc. Since increasing the amount of lipids only caused
135 elongation of the nanodisc in one direction without a change in its diameter near the subunit cavity,
136 we proceeded with data collection on the sample with the lowest LPR of 145:1, which resulted in
137 a homogeneous assembly of approximately 165 x 140 Å in size (Figure 2-figure supplement 1A).
138 This approach was used to determine the structures of ligand-bound and ligand-free states of
139 nhTMEM16 in a membrane-like environment. The data is of excellent quality and provide an
140 unambiguous view of nhTMEM16 in different conformations (Figures 2 and 3; Figure 2-figure
141 supplements 2; Figure 3-figure supplements 1-2; Tables 1 and 2).

142 The differences between structures of nhTMEM16 determined in detergents and in a lipid
143 environment are most pronounced for the Ca^{2+}-free state determined at 3.8 Å resolution (Figure
144 2A,B,D; Figure 2-figure supplement 2). Whereas the structure in detergent displays a Ca^{2+}-free
145 conformation where the subunit cavity remains open to the membrane, the same region has
146 changed its accessibility in the nanodisc sample. Here, the movement of α4 leads to a shielding of
147 the cavity from the membrane core, resembling a conformation observed in the ion channel
148 TMEM16A (Figure 2E) (Dang et al., 2017; Paulino et al., 2017a; Paulino et al., 2017b). This
149 movement is accompanied by a conformational change of α6 as a consequence of the repulsion of
150 negatively charged residues in the empty Ca^{2+}-binding site (Figure 2B-D). Generally, the Ca^{2+}-
151 free state of nhTMEM16 in nanodiscs is very similar to equivalent structures of its close homologs
152 afTMEM16 (Falzone et al., 2019), TMEM16K (Bushell et al., 2018) and the more distantly related
153 scramblase TMEM16F (Alvadia et al., 2018) (Figure 2C,F and Figure 1-figure supplement 4), thus
154 underlining that all structures represent inactive conformations of the scramblase in the absence of
155 ligand.
156
157 **Structures of Ca^{2+}-bound states of nhTMEM16 in lipid nanodiscs**
158 Different from the data of the Ca^{2+}-free protein in nanodiscs, which comprises a single prevailing
159 state, the cryo-EM data obtained for the Ca^{2+}-bound samples in the same environment shows a
160 large heterogeneity along the 'subunit cavity'. This heterogeneity allows to sample the transition
161 of the lipid permeation path from the closed to the open state and emphasizes the intrinsic dynamics
162 of this region during activation (Figure 3; Figure 3-figure supplements 1 and 2; Table 2). A
163 classification of the data yielded several states with distinct conformations of the 'subunit cavity',
164 all of which exhibit well-resolved cryo-EM density for two Ca^{2+} ions and a rigid arrangement of

165 α6 in place to coordinate the divalent ions (Figure 3A-C; Figure 3-figure supplements 1 and 2).
166 About 50% of the particles define classes where α3 and α4 are poorly resolved, thus emphasizing
167 the high degree of flexibility in the region, which suggest that several states along the activation
168 process might be transient (classes 5 and 6, Figure 3-figure supplement 1C). By contrast, three
169 classes show well resolved distinct conformations. The 'open' class, at 3.6 Å resolution,
170 encompasses about 25% of the particles and strongly resembles the Ca^{2+}-bound open state obtained
171 in detergent, with a subunit cavity that is exposed to the membrane (Figure 3A; Figure 3-figure
172 supplements 1 and 2). In contrast, the 'Ca^{2+}-bound closed' class determined from 15% of particles
173 at 3.6 Å resolution, strongly resembles the 'Ca^{2+}-free closed' state obtained in nanodiscs, with a
174 subunit cavity that is shielded from the membrane, except that Ca^{2+} is bound and α-helix 6 is less
175 mobile (Figure 3C,G; Figure 3-figure supplements 1 and 2). The third distinct state at 3.7 Å
176 resolution encompasses 12% of all particles and shows an 'intermediate' conformation, where the
177 subunit cavity is still shielded from the membrane but where a potential aqueous pore surrounded
178 by α-helices of the subunit cavity has widened compared to the closed state (Figure 3B,E,F; Figure
179 3-figure supplements 1 and 2). The distribution of states, with a portion of nhTMEM16 residing
180 in potentially non-conductive conformations correlates with the lower activity of the protein in this
181 lipid composition (Figure 1-figure supplement 1C) and it emphasizes the equilibrium between
182 conformations of nhTMEM6 in the Ca^{2+}-bound state. Unassigned weak density in the subunit
183 cavity in the 'open' - but not in the 'closed' - conformation, hints at lipid molecules during the
184 transition between the leaflets (Figure 3-figure supplement 3). Strikingly, the strongest density is
185 located at an equivalent position as found for the potential DDM density in the cryo-EM maps of
186 nhTMEM6 in detergent (Figure 1-figure supplement 5).
187

188 **Conformational transitions**

189 The diversity of conformations of nhTMEM16 observed in various datasets and the presence of
190 different populations in the Ca^{2+}-bound sample in lipid nanodiscs suggest that our structures
191 represent distinct states along a stepwise activation process. Apart from a small rearrangements of
192 the cytosolic domain, the core of the protein is virtually identical in all structures and the largest
193 movements are observed in the vicinity of the subunit cavity (Figures 2D, 3D-G 4 and 5A and
194 Video 1). The Ca^{2+}-bound conformation in detergent and the 'open' class observed in the data of
195 Ca^{2+}-bound protein in nanodiscs, both show the widest opening of the subunit cavity and thus
196 likely depict a scrambling-competent state of the protein (Figure 4A). In this open state, α-helices
197 4 and 6 are separated from each other on their entire length framing the two opposite edges of a
198 semicircular polar furrow that is exposed to the lipid bilayer (Figure 4A). In this case, the
199 interaction of α3 with α10 of the adjacent subunit on the intracellular side appears to limit the
200 movement of α4, thus preventing a further widening of the cavity on the intracellular side (Figures
201 5A-C). On the opposite border of the subunit cavity, α6 is immobilized in its position by the bound
202 Ca^{2+} ions, which results in a tight interaction with α7 and α8 (Figure 5D). In the 'intermediate'
203 class found in the Ca^{2+}-bound sample in nanodiscs, we find marked conformational changes
204 compared to the 'open state'. The most pronounced differences are found for the α3-α4 pair. The
205 intracellular part of α3 (but not the α2-α3 loop contacting the helix Cα1 following α10) has
206 detached from its interaction with α10, leading to a concomitant movement of α4 at the same
207 region (Figure 5B). This movement has also affected the conformation of the extracellular part of
208 α4, which has rotated and approached α6, thereby forming initial contacts between both helices
209 (Figures 4B and 5C,D). The subunit cavity in this conformation is no longer exposed to the
210 membrane at its extracellular part and the structure likely represents an intermediate of the

211 scramblase towards activation (Figure 4B). This 'intermediate state' is remarkable in light of the
212 observed ion conduction of nhTMEM16 and other TMEM16 scramblases (Alvadia et al., 2018;
213 Lee et al., 2016; Suzuki et al., 2013; Yang et al., 2012; Yu et al., 2015), as it might harbor a
214 potential protein-enclosed aqueous pore located in region that is expanded compared to the 'closed
215 state' (Figure 5-figure supplement 1). The interactions between α4 and α6 on the extracellular side
216 further tighten in the 'closed' class found in the Ca^{2+}-bound sample in nanodiscs, thereby
217 constricting the aqueous pore observed in the 'intermediate state' (Figures 4C; Figure 5-figure
218 supplement 1). This conformation strongly resembles the Ca^{2+}-free 'closed' conformation
219 observed in nanodiscs, except that in the latter, the dissociation of the ligand from the protein has
220 allowed a relaxation of α6 leading to its detachment from α8 at the intracellular part of the helix
221 (Figures 4D and 5C,D). Although, unlike TMEM16A and TMEM16F, nhTMEM16 does not
222 contain a flexible glycine residue at the hinge, the movements of α6 upon Ca^{2+}-release occur at a
223 similar region (Alvadia et al., 2018; Paulino et al., 2017a) (Figure 2C-F and Figure 1-figure
224 supplement 4). In the transition from an 'open' to a 'closed state', α4 undergoes the largest changes
225 among all parts of nhTMEM16 with two prolines (Pro 332 and Pro 341) and a glycine (Gly 339)
226 serving as potential pivots for helix-rearrangements (Figure 5E and Video 1). Remarkably, both
227 prolines are conserved among fungal homologues and Pro 332 is also found in TMEM16K
228 (Bushell et al., 2018), the closest mammalian orthologue of nhTMEM16 (Figure 1-figure
229 supplement 4).
230
231 **Protein-induced distortion of the lipid environment**
232 A remarkable feature observed in the cryo-EM maps concerns the arrangement of detergent or
233 lipid molecules surrounding nhTMEM16, which allowed us to characterize the influence of the

234 protein on its environment. The observed distortions are found to a similar extent in all determined
235 structures, irrespective of the presence or absence of calcium in detergent or lipid nanodiscs and
236 can thus be considered a state-independent property of the protein. Neither detergent molecules
237 nor nanodisc lipids are uniformly distributed on the outside of nhTMEM16 (Figure 6 and Video
238 2). Instead, they adapt to the shape of the protein with distortions observed in the vicinity of the
239 shorter α-helices 1 and 8 at the extracellular side and at the gap between α-helices 4 and 6 at the
240 intracellular side (Figure 6). These distortions result in a marked deviation from the annular shape
241 of detergents molecules or lipids surrounding the protein found in most membrane proteins.
242 Remarkably, the resulting undulated distribution contains depressions in both the detergent and
243 lipid density close to the entrances of the subunit cavity (Figure 6 and Video 2). The arrangement
244 of the protein with its long dimension parallel to the short diameter of the oval-shaped nanodiscs
245 reflects the preferential location of lipids at sites distant from the subunit cavity (Figure 2-figure
246 supplement 1). The protein affects the distribution of lipids and the shape of the plane of the bilayer
247 in nanodiscs, which is slightly V-shaped and locally deviates from planarity at several regions
248 (Figure 6B,C). These pronounced depressions thin and distort the lipid structure at both ends of
249 the subunit cavity, thereby likely facilitating the entry of polar head-groups into the cavity and
250 lowering the barrier for lipid movement (Figure 6B).
251
252 **Functional properties of mutants affecting the activation process**
253 The distinct conformations of nhTMEM16 determined in this study hint at a sequential
254 mechanism, in which Ca^{2+}-dependent and independent steps are coupled to promote activation
255 similar to ligand-dependent ion channels. We have thus investigated the functional consequences
256 of mutations of residues of the Ca^{2+}-binding site and of the hinges for α4 movement with our

257 liposome-based lipid scrambling assay. The mutation D503A located on α7 concerns a residue of
258 the Ca^{2+}-binding site that does not change its position in different protein conformations and thus
259 should affect the initial ligand-binding step (Figure 7A). In this case, we find a Ca^{2+}-dependent
260 scrambling activity, although with strongly decreased potency of the ligand (Figures 7B,C). Next,
261 we investigated whether the mutation of two proline residues and a close-by glycine (Pro 332, Gly
262 339 and Pro 341), which form potential pivots during the rearrangement of α4 would affect lipid
263 scrambling (Figure 7A). Whereas we did not find any detectable effect in the mutant P341A, the
264 mutants G339A and P332A showed a strongly decreased activity both in the presence and absence
265 of Ca^{2+} (but no detectable change in the Ca^{2+}-potency of the protein, Figures 7D-F; Figure 7-figure
266 supplement 1). As the residues do not face the subunit cavity in the 'open state' and are unlikely
267 to interact with translocating lipids, we assume that these mutants alter the equilibrium between
268 active and inactive conformations thus emphasizing the role of conformational changes in α-helix
269 4 for nhTMEM16 activation.
270
271 **Discussion**
272 By combining data from cryo-electron microscopy and biochemical assays, our study has
273 addressed two important open questions concerning the function of a TMEM16 scramblase: it has
274 revealed the conformational changes that lead to the activation of the protein in response to Ca^{2+}
275 binding and it has shown how the protein interacts with the surrounding membrane to facilitate
276 lipid translocation. Structures in Ca^{2+}-free and bound states reveal distinct conformations of
277 nhTMEM16, which capture the catalytic subunit cavity of the scramblase at different levels of
278 exposure to the membrane during the activation process, representing a 'closed', at least one
279 'intermediate' and an 'open state'. As different protein conformations are observed in presence

280 and absence of its ligand, we propose a stepwise activation mechanism for TMEM16 scramblases,
281 where all states are at equilibrium (Figure 8; Figure 8-figure supplement 1). Here, the Ca^{2+}-free
282 conformation obtained in nanodiscs defines a non-conductive state of the protein, where the polar
283 subunit cavity is shielded from the membrane by tight interactions of α4 and α6 on the extracellular
284 part of the membrane (Figure 4D). The protein surface of the closed subunit cavity is hydrophobic
285 as expected for a membrane protein. This 'closed state' of nhTMEM16 resembles equivalent
286 structures obtained for the closely related lipid scramblases afTMEM16 (Falzone et al., 2019),
287 TMEM16K (Bushell et al., 2018), the more distantly related TMEM16F (Alvadia et al., 2018) and
288 the ion channel TMEM16A (Figure 2E,F) (Dang et al., 2017; Paulino et al., 2017a; Paulino et al.,
289 2017b), thus underlining that it is representative for an inactive conformation of both functional
290 branches of the family. In this conformation, the Ca^{2+}-binding site is empty, with the intracellular
291 part of α6 positioned apart from the remainder of the binding site to release the electrostatic strain
292 induced by the large negative net-charge in this region. Details of the conformation of α6 in the
293 absence of Ca^{2+} differ between the family members of known structure with the conformation in
294 nhTMEM16 being closer to the one observed for TMEM16F (Alvadia et al., 2018; Paulino et al.,
295 2017a).
296 During the activation process, Ca^{2+} binding provides interactions with residues on α6. The helix
297 rearranges into a locked state, as manifested in the well resolved cryo-EM density for its
298 intracellular half, which shields the binding site from the cytoplasm. This Ca^{2+}-induced movement
299 of α6 in nhTMEM16 is coupled to rearrangements in its interface with α4, potentially weakening
300 the interactions and resulting in a widening of the cavity. A cavity with a changed accessibility to
301 the membrane is displayed in a population of particles observed in the Ca^{2+}-bound nhTMEM16
302 structure in nanodiscs (Figure 4B). As the subunit cavity is not yet exposed to the membrane, the

303 ‘intermediate state’ likely does not promote lipid scrambling. Instead, it might have opened a
304 protein-enclosed pore that could facilitate ion conduction (Figure 5-figure supplement 1), which
305 has been described as by-product of lipid scrambling in nhTMEM16 (Lee et al., 2016) and which
306 is a hallmark of the lipid scramblase TMEM16F (Alvadia et al., 2018; Yang et al., 2012; Yu et al.,
307 2015). Following the initial Ca^{2+}-induced conformational transition, the activation of lipid
308 scrambling requires a second step, which leads to a larger reorientation of α-helices 3 and 4 and a
309 subsequent opening of the polar subunit cavity to the membrane (Figures 3 and 4). This open state
310 is defined by the Ca^{2+}-bound structure of nhTMEM16 obtained in detergent and by one of the
311 classes observed in the Ca^{2+}-bound nanodisc dataset.
312 Thus, ion conduction and lipid-scrambling in nhTMEM16 and other TMEM16 scramblases might
313 be mediated by distinct conformations which are at equilibrium in a Ca^{2+}-bound protein (Figure 8;
314 Figure 8-figure supplement 1). This stepwise activation mechanism is in general accordance with
315 molecular dynamics simulations, which have started from the fully Ca^{2+}-bound open structure and
316 for which transitions leading to a partial closure of the subunit cavity have been observed in the
317 trajectories (Jiang et al., 2017; Lee et al., 2018). The basal scrambling activity of nhTMEM16 is
318 likely a consequence of the equilibrium between open, intermediate and closed conformations,
319 which is strongly shifted towards the closed state in the absence of Ca^{2+}. This is consistent with
320 the observation of a Ca^{2+}-free open state in detergent but not in nanodiscs, where the detergent
321 environment favors the equilibrium towards the open conformation (Figure 1H).
322 The cryo-EM structures of nhTMEM16 also reveal how the protein interacts with the surrounding
323 membrane to disturb its structure and consequently lower the energy barrier for lipid flip-flop, as
324 predicted from molecular dynamics simulations (Bethel and Grabe, 2016; Jiang et al., 2017; Lee
325 et al., 2018; Stansfeld et al., 2015). Our data reveal a pronounced distortion of the protein-

326 surrounding environment, which is stronger than observed for the ion channel TMEM16A (Paulino
327 et al., 2017b). This effect is preserved in all four datasets, irrespectively of the presence or absence
328 of ligand in detergent or nanodiscs, as their underlying structural features change little in the
329 different conformations. The distortion causes a deviation of the detergent or lipid molecules
330 surrounding nhTMEM16 from the annular structure observed in most membrane proteins (Figure
331 6 and Video 2). The resulting deformation of the membrane at the entrances to the subunit cavity
332 potentially serves to channel lipid headgroups through this hydrophilic furrow on their way across
333 the membrane.
334 In summary, our structures of nhTMEM16 have described how a calcium-activated lipid
335 scramblase is activated in a stepwise manner and how it bends the surrounding bilayer to promote
336 the transport of lipids between both leaflets of the membrane by a mechanism that is likely
337 conserved within the family.
338
339

340 **Materials and methods**

341 **Key resources table**

Reagent or Resource	Source	Identifier
Antibodies		
Mouse monoclonal Anti-c-Myc	Millipore Sigma	Cat#M4439; Clone#9E10
Peroxidase Affinipure goat anti-mouse IgG	Jackson Immunoresearch	Cat#115-035-146
Chemicals, Peptides, and Recombinant Proteins		
n-dodecyl-β-d-maltopyranoside (DDM), Solgrade	Anatrace	Cat#D310S
Water for molecular biology	Millipore	H20MB1006
Calcium nitrate tetrahydrate	Millipore Sigma	Cat#C4955
Sodium chloride	Millipore Sigma	Cat#71380
Magnesium chloride	Fluka	Cat#63065
HEPES	Millipore Sigma	Cat#H3375
Ethylene glycol-bis(2-aminoethylether)-N,N,N′,N′-tetraacetic acid	Millipore Sigma	Cat#03777
Ethylenediaminetetraacetic acid	Millipore Sigma	Cat#E6758

cOmplete, EDTA-free Protease Inhibitor Cocktail	Roche	Cat#5056489001
Biotin	Millipore Sigma	Cat#B4501
D-desthiobiotin	Millipore Sigma	Cat#D1411
Amicon Ultra-4 - 100 KDa cutoff	EMD Millipore	Cat#UFC8100
0.22 µm Ultrafree-MC Centrifugal Filter	EMD Millipore	Cat#UFC30GV
Glycerol	Millipore Sigma	Cat#G5516
1-palmitoyl-2-oleoyl-glycero-3-phosphocholine	Avanti Polar Lipids, Inc	Cat#850457C
1-palmitoyl-2-oleoyl-sn-glycero-3-phospho-(1'-rac-glycerol)	Avanti Polar Lipids, Inc	Cat#840457C
Diethyl ether	Millipore Sigma	Cat#296082
Bio-Beads SM-2 Adsorbents	Bio-Rad	Cat# 1523920
E. coli polar lipid extract	Avanti Polar Lipids, Inc	Cat#100600C
Egg PC, 95%	Avanti Polar Lipids, Inc	Cat#131601C
18:1-06:0 NBD-PE	Avanti Polar Lipids, Inc	Cat#810155C
Potassium chloride	Millipore Sigma	Cat#746436

CHAPS	Millipore Sigma	Cat#C3023
Sodium dithionite	Millipore Sigma	Cat#157953
Yeast nitrogen base without amino acids	Millipore Sigma	Cat#Y0626
Yeast Synthetic Drop-out Medium Supplements without uracil	Millipore Sigma	Cat#Y1501
D-Glucose	Applichem	Cat#A1422
Galactose	Millipore Sigma	Cat#G0625
Lithium acetate	Millipore Sigma	Cat#L4158
PEG3350	Millipore Sigma	Cat#88276
DNAse I	AppliChem	A3778-0500
HRV 3C protease	Raimund Dutzler laboratory	NA
Critical Commercial Assays		
Pierce Streptavidin Plus UltraLink Resin	Thermo Fisher Scientific	Cat#53117
Strep-Tactin® Superflow® high capacity	IBA Lifesciences	Cat#2-1208-010
Superdex 200 10/300 GL	GE Healthcare	Cat# 17-5175-01
Superose 6 10/300 GL	GE Healthcare	Cat#17-5172-01
Deposited Data		

Cryo-EM map and model of nhTMEM16 DDM +Ca^{2+}	This study	EMD-XXX, PDB ID XXXX
Cryo-EM map and model of nhTMEM16 DDM -Ca^{2+}	This study	EMD-XXX, PDB ID XXXX
Cryo-EM map and model of nhTMEM16 2N2 nanodiscs +Ca^{2+}	This study	EMD-XXX, PDB ID XXXX
Cryo-EM map and model of nhTMEM16 2N2 nanodiscs -Ca^{2+}	This study	EMD-XXX, PDB ID XXXX
Experimental Models: strains		
S. cerevisiae FGY217	David Drew laboratory	NA
Recombinant DNA		
nhTMEM16 open reading frame	GenScript	PubMed accession number XM_003045982
Yeast expression vector with N-terminal streptavidin binding peptide, Myc tag and 3C protease cleavage site	Raimund Dutzler laboratory	NA
Membrane scaffold protein (MSP) 2N2	Stephen Sligar laboratory	Addgene:Cat#29520
Software and Algorithms		

Online WEBMAXC calculator	Bers et al., 2010	http://maxchelator.stanford.edu/webmaxc/webmaxcS.htm
Focus 1.1.0	Biyani et al., 2017	https://focus.c-cina.unibas.ch/about.php
MotionCorr2 1.1.0	Zheng et al., 2017	http://msg.ucsf.edu/em/software/motioncor2.html
CTFFIND 4.1	Rohou et al., 2015	http://grigoriefflab.janelia.org/ctf
Relion v 2.1 and 3.0	Kimanius et al., 2016	https://www2.mrc-lmb.cam.ac.uk/relion/
Phenix 1.14	Adams et al., 2010	http:// http://phenix-online.org/
Coot 0.8.9.1	Emsley et al., 2004	https://www2.mrc-lmb.cam.ac.uk/personal/pemsley/coot/
Pymol 2.0	Schrodinger LLC	https://pymol.org/2/
Chimera 1.12	Pettersen et al., 2004	https://www.cgl.ucsf.edu/chimera/
ChimeraX 0.6	Goddard et al., 2018	https://www.rbvi.ucsf.edu/chimerax/

Other		
Whatman® Nuclepore™ Track-Etched Membranes diam. 19 mm, pore size 0.4 µm, polycarbonate	Millipore Sigma	Cat#WHA800282
HPL6	Maximator	NA
Fluoromax 4	Horiba	NA
300 mesh Au 1.2/1.3 cryo-EM grids	Quantifoil	Cat#N1-C14nAu30-01

342

343

344

345 **Strains**

346 Wild type *S. cerevisiae* FGY217 were grown either on YPD agar or in YPD liquid media
347 supplemented with 2% glucose at 30 °C. After the transformation with respective plasmids, the
348 cells were grown on yeast synthetic drop-out media without uracil with 2% glucose at 30 °C. For
349 protein expression, the cells were transferred into a selective media containing 0.1% glucose.

350

351 **Construct preparation**

352 The sequence encoding nhTMEM16 was cloned into a modified FX-cloning compatible (Geertsma
353 and Dutzler, 2011) pYES2 vector as a C-terminal fusion to streptavidin-binding peptide (SBP) and
354 Myc tags that were followed by an HRV 3C cleavage site. The mutations were introduced using a
355 QuickChange method (Zheng et al., 2004).

356

357 **Protein expression and purification**

358 All buffers were prepared using Ca^{2+}-free water for molecular biology (Millipore). Plasmids
359 carrying the WT or mutant genes were transformed into the *S. cerevisiae* FGY217 strain as
360 described (Gietz and Schiestl, 2007) using lithium acetate/single-stranded carrier
361 DNA/polyethylene glycol method. The cells carrying the plasmid were grown at 30 °C in a yeast
362 synthetic dropout media until the culture reached the OD_{600} of 0.8. Afterwards, the protein
363 expression was initialized by adding 2% galactose and the temperature was decreased to 25 °C.
364 The protein was expressed for 40 hours after induction. Cells were harvested at 7,200 *g* for 10 min
365 and resuspended in buffer A (50 mM HEPES pH 7.6, 150 mM NaCl, 10 mM EGTA) containing
366 1 mM $MgCl_2$, DNAse and protease inhibitor cocktail tablets and lysed using a high pressure cell
367 lyser HPL6 at 40 KPsi. Cell-debris was removed by centrifugation at 8,000 *g* for 30 min.
368 Membranes were subsequently harvested by centrifugation with a 45 TI rotor (Beckmann) at
369 200,000 *g* for 1.5 hours, resuspended in buffer A containing 5% glycerol and flash-frozen in liquid
370 N_2 and stored at -80 °C until further use. During purification, all steps were carried out at 4 °C or
371 on ice. For purification, different amount of membrane vesicles were used depending on the
372 purpose of the experiment: 30 g of membranes were used for sample preparation for cryo EM in
373 detergent and in nanodiscs each, and 10 g of membranes for functional assays. Membranes were
374 solubilized in buffer A containing 2% *n*-dodecyl-β-d-maltopyranoside (DDM) and 5% glycerol
375 for 1.5 h. The insoluble fraction was removed by ultracentrifugation at 200,000 *g* for 30 min. The
376 supernatant was applied to 4 ml of streptavidin Ultralink resin for 1.5 h, incubated under gentle
377 agitation. The resin containing bound protein was subsequently washed with 50 column volumes
378 (CV) of buffer B (10 mM HEPES pH 7.6, 150 mM NaCl, 5 mM EGTA, 0.03% DDM, 5%
379 glycerol).

380 For sample preparation for cryo-EM in detergent, the purification tag was cleaved on the resin
381 with 2.4 mg of HRV 3C protease in buffer B containing 20 μg/ml of yeast polar lipids for 2 h. The
382 flow-through was collected, concentrated using 100 kDa cut-off centrifugal filter units at 700 *g*
383 and injected onto a Superdex 200 size-exclusion column equilibrated in buffer C (5 mM HEPES
384 pH 7.6, 150 mM NaCl, 2 mM EGTA, 0.03% DDM). Main peak fractions were pooled and
385 concentrated to 3.3 mg/ml as described above.
386 For sample preparation in lipid nanodiscs, membrane scaffold protein (MSP) 2N2 was expressed
387 and purified as described (Ritchie et al., 2009), except that the polyhistidine-tag was not removed.
388 Chloroform-solubilized lipids (POPC:POPG at a molar ratio of 7:3) were pooled, dried under a
389 nitrogen stream and washed twice with diethyl ether. The resulting lipid film was dried in a
390 desiccator overnight, and solubilized in 30 mM DDM at a final lipid concentration of 10 mM.
391 nhTMEM16 was purified as described above using the same amount of streptavidin resin, except
392 that the uncleaved fusion construct was eluted from the beads with buffer B containing 3 mM
393 biotin. Protein-containing fractions were pooled and concentrated as described above. Biotin was
394 removed from the sample via gel filtration on a Superdex 200 column. Purified protein was
395 assembled into 2N2 nanodiscs at three different molar ratios of protein:lipids:MSP (*i.e.* 2:725:10,
396 2:775:10, and 2:1100:10) as described (Ritchie et al., 2009). This procedure resulted in a five-fold
397 excess of empty nanodiscs, which prevented multiple incorporations of target proteins into a single
398 nanodisc. nhTMEM16 was mixed with detergent-solubilized lipids and incubated for 30 min on
399 ice. Subsequently, purified 2N2 was added to the sample, and the mixture was incubated for an
400 additional 30 min. Detergent was removed by incubating the sample overnight with SM-2 biobeads
401 (200 mg of beads/ml of the reaction) under constant rotation. From this point on, detergent was
402 excluded from all buffers. To separate the protein-containing from empty nanodiscs, the sample

403 was incubated with 1 ml of streptavidin resin for 1.5 hours. The resin was washed with 10 CV of
404 buffer B and assembled nanodiscs containing nhTMEM16 were eluted in buffer B containing 3
405 mM biotin. The purification tag was removed by incubation with 0.8 mg of HRV 3C protease for
406 2 hours. Cleaved samples were concentrated at 500 *g* using concentrators (Amicon) with a
407 molecular weight cut-off of 100 kDa and injected onto a Superose 6 column equilibrated in buffer
408 C. Analogously to the detergent sample, the main peak fractions were concentrated to around 2
409 mg/ml.
410 For reconstitution into proteoliposomes, nhTMEM16 was purified as described for detergent
411 samples used for cryo-EM with minor differences: lysate was incubated with 3 ml of streptactin
412 resin and eluted in buffer B containing 5 mM of d-desthiobiotin and the purification tag was not
413 removed.
414
415 **Reconstitution into the liposomes and scrambling assay**
416 Functional reconstitution was carried out essentially as described (Malvezzi et al., 2013). Lipids
417 for the reconstitution *(E. coli* polar extract and egg-PC at a ratio of 3:1 (w/w) was supplemented
418 with 0.5% (w/w) 18:1-06:0 NBD-PE) were pooled and dried as described above. The lipid film
419 was dissolved in assay buffer A (20 mM HEPES pH 7.5, 300 mM KCl, 2 mM EGTA) containing
420 35 mM CHAPS at a final lipid concentration of 20 mg/ml, aliquoted, flash-frozen and stored until
421 further use. Soy bean lipids extract with 20% cholesterol were prepared as described in Alvadia et
422 al, 2018. On the day of reconstitution, lipids were diluted to 4 mg/ml in assay buffer A and purified
423 protein was added to the lipid mixture at a lipid to protein ratio of 300:1 (w/w). As a control, an
424 equivalent volume of the gel filtration buffer was added to aliquots from the same batch of lipids
425 and treated the same way as the proteoliposomes sample, resulting in the assembly of empty

426 liposomes. Soy bean lipid mixture was destabilized with Triton X-100 as described in Alvadia et
427 al, 2018. The mixture was incubated for 15 min at room temperature (RT). Biobeads (15 mg of
428 beads/mg of lipids) were added 4 times (after 15 min, 30 min, 1 h and 12 h). After the second
429 addition of biobeads, the sample was transferred to 4 °C. The proteoliposomes were harvested by
430 centrifugation (150,000 *g*, 30 min, 4 °C), resuspended in assay buffer A containing desired
431 amounts of free Ca^{2+} (calculated with the WEBMAXC calculator) at a final concentration of 10
432 mg/ml in aliquots of 250 µl, flash-frozen and stored at -80 °C until further use. To characterize the
433 protein activity in the lipid mix used for the preparation of nanodisc samples, nhTMEM16 was
434 reconstituted into liposomes composed of 7 POPC:3 POPG (mol/mol) with 0.5 % 18:1-06:0 NBD-
435 PE. For conditions mimicking a eukaryotic membrane, the protein was reconstituted in soybean
436 polar lipids extract with 20% cholesterol (w/w) and 0.5% 18:1-06:0 NBD-PE. Each mutant was
437 purified and reconstituted independently three times on three different days (defined as distinct
438 biological replicate). To correct for differences in the reconstitution efficiency, WT was included
439 alongside with the mutants into each experiment, and reconstituted into the same batch of lipids
440 on the same day. Reconstitution of the WT into nanodisc lipids and soy bean lipids was performed
441 once.

442 On the day of the measurement, 250 µl aliquots of liposomes were frozen and thawed 3 times and
443 extruded 21 times through a 400 nm polycarbonate membrane using LipoFast extruder (Avestin).
444 Scrambling data was recorded on a Horiba Fluoromax spectrometer. For the measurement,
445 liposomes were diluted to 0.2 mg/ml in assay buffer B (80 mM HEPES pH 7.5, 300 mM KCl, 2
446 mM EGTA) containing corresponding amounts of free Ca^{2+}. odium dithionite was added after 60
447 sec to a final concentration of 30 mM and the fluorescence decay was recorded for additional 340
448 sec. Traces with deviations in fluorescence values of more than $0.03x10^6$ counts per second within

449 the first 60 s of the measurement or displaying uncharacteristic spikes in fluorescence decay after
450 addition of dithionite were discarded. Each sample was measured three times (technical replicate).
451 Data were normalized as F/Fmax.

452 Under ideal conditions, all liposomes should be unilammelar and the lipid composition of the two
453 leaflets of the bilayer should be symmetric. Such scenario would result in a 50% fluorescence
454 decrease upon addition of dithionite to the outside of empty liposomes and a full decay of the
455 fluorescence in liposomes containing an active scramblase, which facilitates lipid flip-flop. In our
456 experiments, we observed fluorescence decays to plateau values ranging between 44–60% in
457 control liposomes and 10-20% in preparations of proteoliposomes containing nhTMEM16
458 constructs due to variabilities in liposome preparation. The incomplete decay is likely a
459 consequence of multilamellar liposomes and due to a fraction of liposomes not containing an active
460 scramblase in proteoliposome preparations. To account for differences in reconstitution efficiency,
461 all protein constructs that are directly compared to each other in our study and that are shown on
462 the same panel were reconstituted with the same batch of lipids on the same day and the analysis
463 is restricted to a phenotypical comparison of the decay kinetics. Reconstitution efficiency of
464 mutants as compared to wild type nhTMEM16 was estimated by Western blotting using a semi-
465 dry transfer protocol. Protein was transferred onto a PVDF membrane (Immobilon-P) and detected
466 using mouse anti-c-Myc antibody (Millipore Sigma) as a primary (1:5,000 dilution) and goat anti-
467 mouse coupled to a peroxidase (Jackson Immunoresearch) as a secondary antibody (1:10,000
468 dilution).

469

470 **Cryo-electron microscopy sample preparation and imaging**

471 2.5 µl of freshly purified protein at a concentration of 3.3 mg/ml when solubilized in DDMand at
472 about 2 mg/ml when reconstituted in nanodiscs were applied on holey-carbon cryo-EM grids
473 (Quantifoil Au R1.2/1.3, 200, 300 and 400 mesh), which were prior glow-discharged at 5 mA for
474 30 s. For datasets of Ca^{2+}-bound protein, samples (containing 2mM EGTA) were supplemented
475 with 2.3 mM $CaCl_2$ 30 minutes before freezing, resulting in a free calcium concentration of 300
476 µM. The pH change in response to the addition Ca^{2+} was monitored and found negligible. Grids
477 were blotted for 2–5 s in a Vitrobot (Mark IV, Thermo Fisher) at 10–15 °C and 100% humidity,
478 plunge-frozen in liquid ethane and stored in liquid nitrogen until further use. Cryo-EM data were
479 collected on a 200 keV Talos Arctica microscope (Thermo Fisher) at the University of Groningen
480 using a post-column energy filter (Gatan) in zero-loss mode, a 20 eV slit, a 100 µm objective
481 aperture, in an automated fashion using EPU software (Thermo Fisher) on a K2 summit detector
482 (Gatan) in counting mode. Cryo-EM images were acquired at a pixel size of 1.012 Å (calibrated
483 magnification of 49,407x), a defocus range from –0.5 to –2 µm, an exposure time of 9 s with a
484 sub-frame exposure time of 150 ms (60 frames), and a total electron exposure on the specimen of
485 about 52 electrons per $Å^2$. The best regions on the grid were screened and selected with an in-
486 house written script to calculate the ice thickness and data quality was monitored on-the-fly using
487 the software FOCUS (Biyani et al., 2017).
488
489 **Image Processing**
490 For the detergent dataset collected in presence of Ca^{2+}, the 2,521 dose-fractionated cryo-EM
491 images recorded (final pixel size 1.012 Å) were subjected to motion-correction and dose-weighting
492 of frames by MotionCor2 (Zheng et al., 2017). The CTF parameters were estimated on the movie
493 frames by ctffind4.1 (Rohou and Grigorieff, 2015). Images showing contamination, a defocus
494 above –0.5 or below –2 µm, or a poor CTF estimation were discarded. The resulting 2,023 images

495 were used for further analysis with the software package RELION2.1 (Kimanius et al., 2016).
496 Around 4,000 particles were initially manually picked from a subset of the dataset and classified
497 to create a reference for autopicking. The final round of autopicking on the whole dataset yielded
498 251,693 particles, which were extracted with a box size of 220 pixels and initial classification steps
499 were performed with two-fold binned data. False positives were removed in the first round of 2D
500 classification. Remaining particles were subjected to several rounds of 2D classification, resulting
501 in 174,901 particles that were further sorted in several rounds of 3D classification. A map created
502 from the X-ray structure of nhTMEM16 (PDBID: 4WIS) was low-pass filtered to 50 Å and used
503 as initial reference for the first round of 3D classification. The resulting best output class was used
504 as new reference in subsequent jobs in an iterative way. The best 3D classes, comprising 128,648
505 particles, were subjected to auto-refinement, yielding a map with a resolution of 4.3 Å. In the last
506 refinement iteration, a mask excluding the micelle was used and the refinement was continued
507 until convergence (focused refinement), which improved the resolution to 4.0 Å. The final map
508 was masked and sharpened during post-processing resulting in a resolution of 3.9 Å. Finally, the
509 newly available algorithms for CTF refinement and Bayesian polishing implemented in Relion3.0,
510 were applied to further improve the resolution (Zivanov et al., 2018). A final round of 3D
511 classification was performed, resulting in 120,086 particles that were subjected to refinement,
512 providing a mask generated from the final PDB model in the last iteration. The final map at 3.6 Å
513 resolution was sharpened using an isotropic B-factor of -126 $Å^2$. While a C1 symmetry was tested
514 and applied throughout image processing workflow, no indication of an asymmetry was identified.
515 Therefore, a C2-symmetry was imposed during the final 3D classification and auto-refinement.
516 Local resolution was estimated by RELION. All resolutions were estimated using the 0.143 cut-
517 off criterion (Rosenthal and Henderson, 2003) with gold-standard Fourier shell correlation (FSC)

518 between two independently refined half maps (Scheres and Chen, 2012). During post-processing,
519 the approach of high-resolution noise substitution was used to correct for convolution effects of
520 real-space masking on the FSC curve (Chen et al., 2013). The directional resolution anisotropy of
521 density maps was quantitatively evaluated using 3DFSC (Tan et al., 2017).
522 For the other datasets, a similar workflow for image processing was applied. In case of the
523 detergent dataset collected in absence of Ca^{2+}, a total of 570,203 particles were extracted with a
524 box size of 240 pixels from 2,947 images. Several rounds of 2D and 3D classification resulted in
525 a final number of 295,219 particles, which yielded a 3.9 Å map after refinement and post-
526 processing. CTF refinement and Bayesian polishing were applied, followed by a second round of
527 CTF refinement. One last round of 3D classification was performed, leading to a final pool of
528 238,070 particles which, after refinement and post processing, resulted in a map at 3.7 Å resolution.
529 For structure determination of nhTMEM16 in lipid nanodiscs, small datasets (around 1000 images)
530 recorded from samples reconstituted at different lipid to protein ratios (LPR) in absence of Ca^{2+}
531 during nanodisc assembly, identified the lowest LPR as optimal condition for large-scale data
532 collection. The dataset in nanodisc in absence of Ca^{2+} resulted in 1,379,187 auto-picked particles
533 from 6,465 images extracted with a box size of 240 pixels, which were reduced to 150,421 particles
534 after several rounds of 2D and 3D classification. CTF refinement and Bayesian polishing followed
535 by a final round of 3D classification was performed, resulting in a selection of 133,961 particles.
536 The final refinement and masking resulted in a 3.8 Å resolution map.
537 Finally, for the dataset in nanodiscs in the presence of Ca^{2+}, 2,440,110 particles were picked from
538 9,426 images and extracted with a box size of 240 pixels. Since the dataset displayed high
539 conformational heterogeneity, C1 symmetry was applied throughout the processing workflow.
540 After several rounds of 2D and 3D classification, the best classes (319,530 particles) were

541 combined and refined. The resulting map was used for CTF refinement in Relion3. Refined
542 particles were subjected to 3D refinement and the obtained map was used to generate a mask for
543 nanodisc signal subtraction. The resulting subtracted particles were used for another round of 3D
544 classification, yielding a subset of 279,609 particles. It was evident from the processing results
545 that the core of the protein was stable and displayed a single conformation, whereas α-helices 3
546 and 4 appeared to be mobile. To separate distinct conformational states, all the particles were
547 aligned using 3D refinement and subsequently subjected to a 3D classification without alignment,
548 using the angles obtained from the preceding refinement job. In one of the resulting classes, the
549 density corresponding to helices 3, 4 and 6 of one of the monomers was not defined, and these
550 particles (11,25%) were thus excluded from further processing. Of the remaining particles, 36,5%
551 are heterogeneous in the region corresponding to α-helices 3 and 4, 14,89% represent nhTMEM16
552 in a closed conformation of the subunit cavity, 11,91% in the intermediate, and two classes
553 (consisting of 15,64% and 9,81% particles respectively) display an open conformation. Each class
554 was subsequently initially refined applying C1 symmetry. Since no difference between the
555 conformations of individual subunits in the dimeric protein was detected, the refinement was
556 repeated with C2 symmetry imposed. The two open classes were merged and refined together.
557 Similar to other datasets, masks generated from PDB models were applied in the last iteration of
558 the refinement. After refinement and post-processing, the resulting resolutions were 3.57 Å for the
559 open class, 3.57 Å for the closed class and 3.68 Å for the intermediate class. We also attempted to
560 classify the heterogeneous class further, but could not improve the separation of the particles. To
561 generate the map of the open conformation containing the nanodisc signal, we reverted the
562 particles from the open class to their original non-subtracted equivalent, and refined them applying
563 C2 symmetry. This map was used to prepare Figure 3-supplement 3, Figure 6 and Video 2.

564

565 **Model building refinement and validation**

566 For the detergent dataset in the presence of Ca^{2+}, the X-ray structure of nhTMEM16 (PDBID:
567 4WIS) was used as a template. The model was manually edited in Coot (Emsley and Cowtan,
568 2004) prior to real-space refinement in Phenix imposing symmetry restraints between subunits
569 throughout refinement (Adams et al., 2010). The higher quality of the cryo-EM density of the
570 cytoplasmic domains compared to the X-ray density allowed for the identification of an incorrect
571 register at the N-terminus of the X-ray structure (PDBID: 4WIS) between residues 20-61. The
572 region comprising residues 15-61 was thus rebuilt. Another change compared to the X-ray
573 structure concerns the remodeled conformation of Lys 598. In several cases the cryo-EM density
574 allowed the interpretation of residues that were not defined in the X-ray structure. These concern
575 residues 130-140 at a loop connecting the cytoplasmic and the transmembrane domain, an extra
576 helical turn at the cytoplasmic side of α6 and residues 476-482 at the loop connecting α6 to α6'.
577 Since residues 690-698 appeared to be helical in the cryo-EM map, the region was rebuilt and it
578 was possible to add the missing residues 688-691. Several regions of the cryo-EM map displayed
579 weaker density compared to the X-ray structure, and hence the residues 416-418, 653-656 and
580 660-663 had to be removed from the model. This corrected nhTMEM16 structure (PDBID: 6QM5)
581 was used for refinement of the nhTMEM16 structure in DDM in the absence of Ca^{2+}, and for
582 model building and refinement of the Ca^{2+}-bound open and Ca^{2+}-bound closed structures in
583 nanodiscs. All models were edited manually in Coot, followed by real space refinement in Phenix.
584 The Ca^{2+}-free structure in DDM (PDBID: 6QM6) and the Ca^{2+}-bound open structure in nanodisc
585 (PDBID: 6QM9) closely resemble the Ca^{2+}-bound structure in DDM, displaying only minor
586 differences. Since the density corresponding to α6 is better resolved in the Ca^{2+}-bound open

587 structure in nanodisc, the helix was extended to Ser 471. The density corresponding to Cα2 of the
588 C-terminus (residues 664-684) was comparably weak in all three open structures and the helix was
589 thus fitted as a rigid body. For the Ca^{2+}-bound closed conformation (PDBID: 6QMB), major
590 changes were introduced for α3, α4 and to a lesser extent for α6. The densities of the loop
591 connecting α5' and α6 and of the cytosolic region of α6 were generally weaker and residues 417-
592 424 and 467-471 were thus not interpreted in this structure. Since the Ca^{2+}-bound closed map in
593 nanodisc displays the highest resolution and quality in the region encompassing α3 and α4, the
594 resulting model was used as a template for the interpretation of the Ca^{2+}-bound intermediate
595 (PDBID: 6QMA) and Ca^{2+}-free (PDBID: 6QM4) structures in nanodisc. In case of the Ca^{2+}-bound
596 intermediate structure, introduced changes are mostly confined to α4, where the extracellular part
597 of the α-helix undergoes a conformational transition towards opening of the subunit cavity. For
598 the Ca^{2+}-free structure in nanodisc, the residues 461-467 of α6 were not modelled due to its high
599 mobility. Figures were prepared using Pymol (The PyMOL Molecular Graphics System, Version
600 2.0 Schrödinger, LLC), Chimera (Pettersen et al., 2004) and ChimeraX (Goddard et al., 2018).
601

602 **Acknowledgments**

603 We thank S. Klauser, S. Rast and M. Punter for their help in establishing the computer
604 infrastructure, H. Stahlberg and K. Goldie at C-Cina of the University of Basel for access to cryo-
605 electron microscopes at an initial stage of the project. S. Weidner and the Workshop of
606 Biochemistry department (UZH) are acknowledged for developing the high-pressure cell lyser. D.
607 Deneka is acknowledged for his advice on nanodisc reconstitution. All members of the Dutzler
608 and Paulino labs are acknowledged for help at various stages of the project.
609

610 **Additional Information**

611 **Funding**

612 **Funder**	**Grant reference number**	**Author**
613 European Research Council	no 339116, AnoBest.	Raimund Dutzler
614 NOW Start-Up grant	no 740.018.016	Cristina Paulino

615 The funders had no role in study design, data collection and interpretation, or the decision to submit
616 the work for publication.

617

618 **Author contributions**

619 V.K. and L.B. purified proteins for cryo-EM and functional characterization. V.K. reconstituted
620 protein into nanodiscs and liposomes and carried out lipid transport experiments. V.K. and C.P.
621 prepared the samples for cryo-EM. V.K., V.C.M., G.T.O. and C.P. collected cryo-EM data. V.K.,
622 V.C.M and C.P. carried out image processing, model building and refinement. V.K., V.C.M, R.D.
623 and C.P. jointly planned experiments, analyzed the data and wrote the manuscript.

624

625 **Additional files**

626

627 **Data availability**

628 The three-dimensional cryo-EM density maps of calcium-free nhTMEM16 in detergent and
629 nanodiscs have been deposited in the Electron Microscopy Data Bank under accession numbers
630 EMD-4589 and EMD-4587, respectively. The maps of calcium-bound samples in detergent and
631 calcium-bound open, calcium-bound intermediate and calcium-bound closed in nanodiscs were

632 deposited under accession numbers EMD-4588, EMD-4592, EMD-4593 and EMD-4594,
633 respectively. The deposition includes the cryo-EM maps, both half-maps, the unmasked and
634 unsharpened refined maps and the mask used for final FSC calculation. Coordinates of all models
635 have been deposited in the Protein Data Bank. The accession numbers for calcium-bound and
636 calcium-free models in detergents are 6QM5 and 6QM6, respectively. The accession numbers for
637 calcium-bound open, calcium-bound intermediate, calcium-bound closed and calcium-free models
638 in nanodiscs are 6QM9, 6QMA, 6QMB and 6QM4, respectively.

639 **References**

640 Adams, P.D., P.V. Afonine, G. Bunkoczi, V.B. Chen, I.W. Davis, N. Echols, J.J. Headd, L.W.
641 Hung, G.J. Kapral, R.W. Grosse-Kunstleve, A.J. McCoy, N.W. Moriarty, R. Oeffner, R.J.
642 Read, D.C. Richardson, J.S. Richardson, T.C. Terwilliger, and P.H. Zwart. 2010. PHENIX:
643 a comprehensive Python-based system for macromolecular structure solution. *Acta*
644 *Crystallogr D Biol Crystallogr*. 66:213-221.

645 Alvadia, C., N.K. Lim, V. Clerico Mosina, G.T. Oostergetel, R. Dutzler, and C. Paulino. 2018.
646 Cryo-EM structures and functional characterization of the lipid scramblase TMEM16F.
647 *bioRxiv*.

648 Bethel, N.P., and M. Grabe. 2016. Atomistic insight into lipid translocation by a TMEM16
649 scramblase. *Proceedings of the National Academy of Sciences of the United States of*
650 *America*. 113:14049-14054.

651 Bevers, E.M., and P.L. Williamson. 2016. Getting to the Outer Leaflet: Physiology of
652 Phosphatidylserine Exposure at the Plasma Membrane. *Physiol Rev*. 96:605-645.

653 Biyani, N., R.D. Righetto, R. McLeod, D. Caujolle-Bert, D. Castano-Diez, K.N. Goldie, and H.
654 Stahlberg. 2017. Focus: The interface between data collection and data processing in cryo-
655 EM. *Journal of structural biology*. 198:124-133.

656 Brunner, J.D., N.K. Lim, S. Schenck, A. Duerst, and R. Dutzler. 2014. X-ray structure of a
657 calcium-activated TMEM16 lipid scramblase. *Nature*. 516:207-212.

658 Brunner, J.D., S. Schenck, and R. Dutzler. 2016. Structural basis for phospholipid scrambling in
659 the TMEM16 family. *Curr Opin Struct Biol*. 39:61-70.

660 Bushell, S.R., A.C.W. Pike, M.E. Falzone, N.J.G. Rorsman, C.M. Ta, R.A. Corey, T.D. Newport,
661 C.A. Shintre, A. Tessitore, A. Chu, Q. Wang, L. Shrestha, S. Mukhopadhyay, J.D. Love,

662 N.A. Burgess-Brown, R. Sitsapesan, P.J. Stansfeld, J.T. Huiskonen, P. Tommaro, A.
663 Accardi, and E.P. Carpenter. 2018. The structural basis of lipid scrambling and inactivation
664 in the endoplasmic reticulum scramblase TMEM16K. *bioRxiv*.
665 Caputo, A., E. Caci, L. Ferrera, N. Pedemonte, C. Barsanti, E. Sondo, U. Pfeffer, R. Ravazzolo,
666 O. Zegarra-Moran, and L.J. Galietta. 2008. TMEM16A, a membrane protein associated
667 with calcium-dependent chloride channel activity. *Science*. 322:590-594.
668 Chen, S., G. McMullan, A.R. Faruqi, G.N. Murshudov, J.M. Short, S.H. Scheres, and R.
669 Henderson. 2013. High-resolution noise substitution to measure overfitting and validate
670 resolution in 3D structure determination by single particle electron cryomicroscopy.
671 *Ultramicroscopy*. 135:24-35.
672 Dang, S., S. Feng, J. Tien, C.J. Peters, D. Bulkley, M. Lolicato, J. Zhao, K. Zuberbuhler, W. Ye,
673 L. Qi, T. Chen, C.S. Craik, Y.N. Jan, D.L. Minor, Jr., Y. Cheng, and L.Y. Jan. 2017. Cryo-
674 EM structures of the TMEM16A calcium-activated chloride channel. *Nature*. 552:426-429.
675 Emsley, P., and K. Cowtan. 2004. Coot: model-building tools for molecular graphics. *Acta*
676 *Crystallogr D Biol Crystallogr*. 60:2126-2132.
677 Falzone, M.E., M. Malvezzi, B.C. Lee, and A. Accardi. 2018. Known structures and unknown
678 mechanisms of TMEM16 scramblases and channels. *The Journal of general physiology*.
679 Falzone, M. E., J. Rheinberger, B.-C. Lee, T. Peyear, L. Sasset, A. Raczkowski, E. Eng, A. Di
680 Lorenzo, O.S. Andersen, C.M. Nimigean, and A. Accardi. 2019. Structural basis of Ca^{2+}-
681 dependent activation and lipid transport by a TMEM16 scramblase. *Elife* **8,** 213.
682 Geertsma, E.R., and R. Dutzler. 2011. A versatile and efficient high-throughput cloning tool for
683 structural biology. *Biochemistry*. 50:3272-3278.

684 Gietz, R.D., and R.H. Schiestl. 2007. High-efficiency yeast transformation using the LiAc/SS
685 carrier DNA/PEG method. *Nat Protoc*. 2:31-34.
686 Goddard, T.D., C.C. Huang, E.C. Meng, E.F. Pettersen, G.S. Couch, J.H. Morris, and T.E. Ferrin.
687 2018. UCSF ChimeraX: Meeting modern challenges in visualization and analysis. *Protein*
688 *Sci*. 27:14-25.
689 Jiang, T., K. Yu, H.C. Hartzell, and E. Tajkhorshid. 2017. Lipids and ions traverse the membrane
690 by the same physical pathway in the nhTMEM16 scramblase. *eLife*. 6.
691 Kimanius, D., B.O. Forsberg, S.H. Scheres, and E. Lindahl. 2016. Accelerated cryo-EM structure
692 determination with parallelisation using GPUs in RELION-2. *eLife*. 5.
693 Kornberg, R.D., and H.M. McConnell. 1971. Inside-outside transitions of phospholipids in vesicle
694 membranes. *Biochemistry*. 10:1111-1120.
695 Lee, B.C., G. Khelashvili, M. Falzone, A.K. Menon, H. Weinstein, and A. Accardi. 2018. Gating
696 mechanism of the extracellular entry to the lipid pathway in a TMEM16 scramblase. *Nat*
697 *Commun*. 9:3251.
698 Lee, B.C., A.K. Menon, and A. Accardi. 2016. The nhTMEM16 Scramblase Is Also a
699 Nonselective Ion Channel. *Biophysical journal*. 111:1919-1924.
700 Malvezzi, M., K.K. Andra, K. Pandey, B.C. Lee, M.E. Falzone, A. Brown, R. Iqbal, A.K. Menon,
701 and A. Accardi. 2018. Out-of-the-groove transport of lipids by TMEM16 and GPCR
702 scramblases. *Proceedings of the National Academy of Sciences of the United States of*
703 *America*.
704 Malvezzi, M., M. Chalat, R. Janjusevic, A. Picollo, H. Terashima, A.K. Menon, and A. Accardi.
705 2013. Ca2+-dependent phospholipid scrambling by a reconstituted TMEM16 ion channel.
706 *Nat Commun*. 4:2367.

707 Milenkovic, V.M., M. Brockmann, H. Stohr, B.H. Weber, and O. Strauss. 2010. Evolution and
708 functional divergence of the anoctamin family of membrane proteins. *BMC Evol Biol*.
709 10:319.
710 Nagata, S., J. Suzuki, K. Segawa, and T. Fujii. 2016. Exposure of phosphatidylserine on the cell
711 surface. *Cell Death Differ*. 23:952-961.
712 Paulino, C., V. Kalienkova, A.K.M. Lam, Y. Neldner, and R. Dutzler. 2017a. Activation
713 mechanism of the calcium-activated chloride channel TMEM16A revealed by cryo-EM.
714 *Nature*. 552:421-425.
715 Paulino, C., Y. Neldner, A.K. Lam, V. Kalienkova, J.D. Brunner, S. Schenck, and R. Dutzler.
716 2017b. Structural basis for anion conduction in the calcium-activated chloride channel
717 TMEM16A. *eLife*. 6.
718 Peters, C.J., J.M. Gilchrist, J. Tien, N.P. Bethel, L. Qi, T. Chen, L. Wang, Y.N. Jan, M. Grabe, and
719 L.Y. Jan. 2018. The Sixth Transmembrane Segment Is a Major Gating Component of the
720 TMEM16A Calcium-Activated Chloride Channel. *Neuron*. 97:1063-1077 e1064.
721 Pettersen, E.F., T.D. Goddard, C.C. Huang, G.S. Couch, D.M. Greenblatt, E.C. Meng, and T.E.
722 Ferrin. 2004. UCSF Chimera--a visualization system for exploratory research and analysis.
723 *J Comput Chem*. 25:1605-1612.
724 Ploier, B., and A.K. Menon. 2016. A Fluorescence-based Assay of Phospholipid Scramblase
725 Activity. *J Vis Exp*.
726 Pomorski, T., and A.K. Menon. 2006. Lipid flippases and their biological functions. *Cell Mol Life*
727 *Sci*. 63:2908-2921.

728 Ritchie, T.K., Y.V. Grinkova, T.H. Bayburt, I.G. Denisov, J.K. Zolnerciks, W.M. Atkins, and S.G.
729 Sligar. 2009. Chapter 11 - Reconstitution of membrane proteins in phospholipid bilayer
730 nanodiscs. *Methods in enzymology*. 464:211-231.
731 Rohou, A., and N. Grigorieff. 2015. CTFFIND4: Fast and accurate defocus estimation from
732 electron micrographs. *Journal of structural biology*. 192:216-221.
733 Rosenthal, P.B., and R. Henderson. 2003. Optimal determination of particle orientation, absolute
734 hand, and contrast loss in single-particle electron cryomicroscopy. *J Mol Biol*. 333:721-
735 745.
736 Sanyal, S., and A.K. Menon. 2009. Flipping lipids: why an' what's the reason for? *ACS Chem Biol*.
737 4:895-909.
738 Scheres, S.H., and S. Chen. 2012. Prevention of overfitting in cryo-EM structure determination.
739 *Nature methods*. 9:853-854.
740 Schroeder, B.C., T. Cheng, Y.N. Jan, and L.Y. Jan. 2008. Expression cloning of TMEM16A as a
741 calcium-activated chloride channel subunit. *Cell*. 134:1019-1029.
742 Smart, O.S., J.G. Neduvelil, X. Wang, B.A. Wallace, and M.S. Sansom. 1996. HOLE: a program
743 for the analysis of the pore dimensions of ion channel structural models. *Journal of*
744 *molecular graphics*. 14:354-360, 376.
745 Stansfeld, P.J., J.E. Goose, M. Caffrey, E.P. Carpenter, J.L. Parker, S. Newstead, and M.S.
746 Sansom. 2015. MemProtMD: Automated Insertion of Membrane Protein Structures into
747 Explicit Lipid Membranes. *Structure*. 23:1350-1361.
748 Suzuki, J., T. Fujii, T. Imao, K. Ishihara, H. Kuba, and S. Nagata. 2013. Calcium-dependent
749 phospholipid scramblase activity of TMEM16 protein family members. *J Biol Chem*.
750 288:13305-13316.

751 Suzuki, J., M. Umeda, P.J. Sims, and S. Nagata. 2010. Calcium-dependent phospholipid
752 scrambling by TMEM16F. *Nature*. 468:834-838.
753 Tan, Y.Z., P.R. Baldwin, J.H. Davis, J.R. Williamson, C.S. Potter, B. Carragher, and D. Lyumkis.
754 2017. Addressing preferred specimen orientation in single-particle cryo-EM through
755 tilting. *Nature methods*. 14:793-796.
756 Whitlock, J.M., and H.C. Hartzell. 2016. Anoctamins/TMEM16 Proteins: Chloride Channels
757 Flirting with Lipids and Extracellular Vesicles. *Annu Rev Physiol*.
758 Williamson, P. 2015. Phospholipid Scramblases. *Lipid Insights*. 8:41-44.
759 Yang, H., A. Kim, T. David, D. Palmer, T. Jin, J. Tien, F. Huang, T. Cheng, S.R. Coughlin, Y.N.
760 Jan, and L.Y. Jan. 2012. TMEM16F forms a Ca2+-activated cation channel required for
761 lipid scrambling in platelets during blood coagulation. *Cell*. 151:111-122.
762 Yang, Y.D., H. Cho, J.Y. Koo, M.H. Tak, Y. Cho, W.S. Shim, S.P. Park, J. Lee, B. Lee, B.M.
763 Kim, R. Raouf, Y.K. Shin, and U. Oh. 2008. TMEM16A confers receptor-activated
764 calcium-dependent chloride conductance. *Nature*. 455:1210-1215.
765 Yu, K., J.M. Whitlock, K. Lee, E.A. Ortlund, Y.Y. Cui, and H.C. Hartzell. 2015. Identification of
766 a lipid scrambling domain in ANO6/TMEM16F. *eLife*. 4:e06901.
767 Zheng, L., U. Baumann, and J.L. Reymond. 2004. An efficient one-step site-directed and site-
768 saturation mutagenesis protocol. *Nucleic Acids Res*. 32:e115.
769 Zheng, S.Q., E. Palovcak, J.P. Armache, K.A. Verba, Y. Cheng, and D.A. Agard. 2017.
770 MotionCor2: anisotropic correction of beam-induced motion for improved cryo-electron
771 microscopy. *Nature methods*. 14:331-332.

772 Zivanov, J., T. Nakane, B. Forsberg, D. Kimanius, W.J.H. Hagen, E. Lindahl, and S.H.W. Scheres.
773 2018. RELION-3: new tools for automated high-resolution cryo-EM structure
774 determination. *bioRxiv*.

775

776 **Figures**

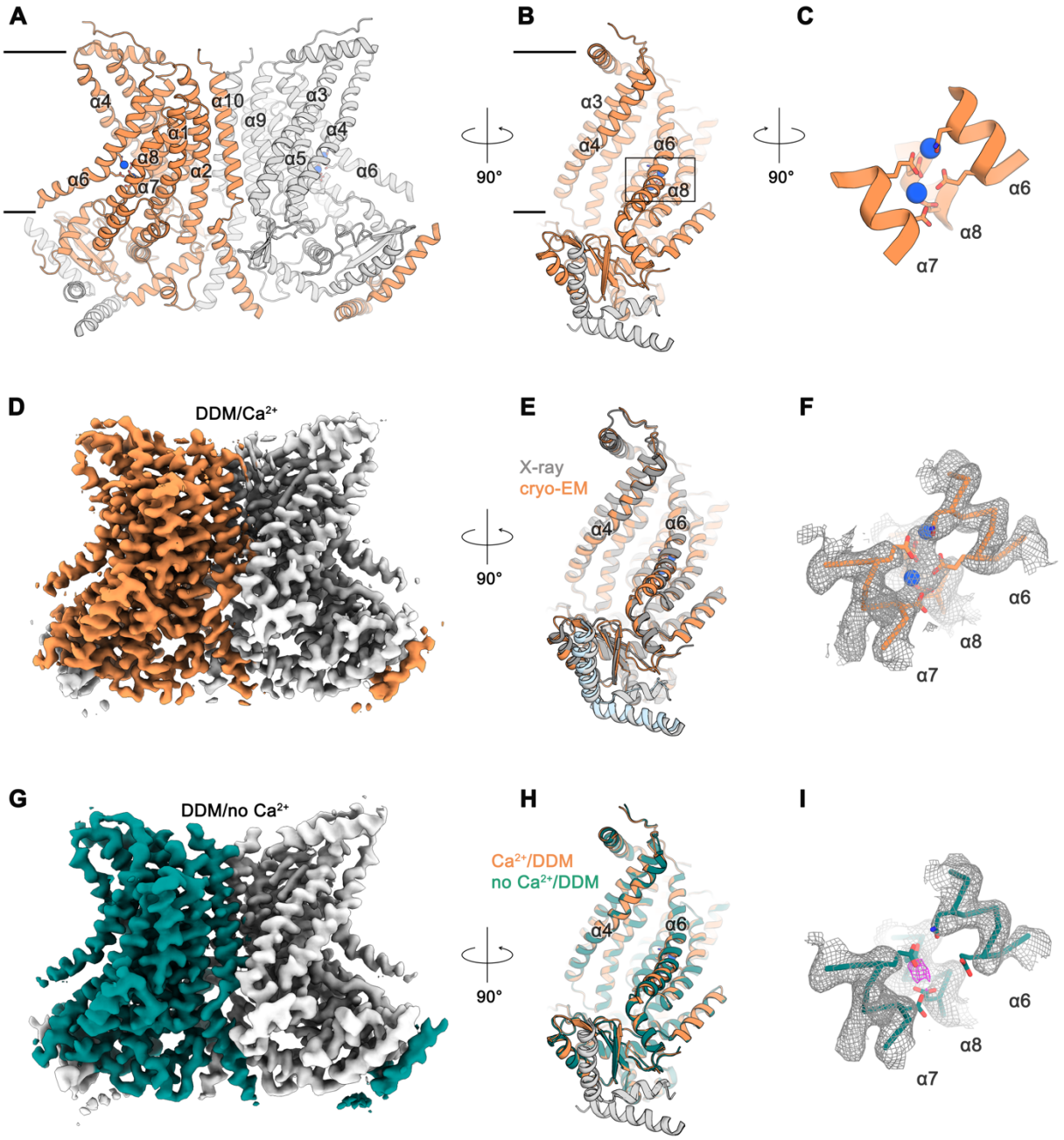

777

778 **Figure 1. Cryo-EM structures of nhTMEM16 in detergent.** Ribbon representation of the Ca^{2+}-
779 bound cryo-EM structure of nhTMEM16 in detergent. The view is from within the membrane
780 perpendicular to the long dimension of the protein (**A**), towards the subunit cavity (**B**) and at the

781 Ca^{2+}-ion binding site (**C**). The membrane boundary is indicated. Subunits in the dimer are depicted
782 in orange and grey, respective transmembrane-helices are labelled and Ca^{2+}-ions are displayed as
783 blue spheres. Relative orientations are indicated and the location of the Ca^{2+}-binding site is
784 highlighted by a box in panel B. (**D**) Cryo-EM map of the nhTMEM16 dimer (orange and grey) in
785 DDM in presence of Ca^{2+} at 3.6 Å sharpened with a b-factor of –126 $Å^2$ and contoured at 6 σ. (**E**)
786 Ribbon representation of a superposition of the Ca^{2+}-bound structure in detergent determined by
787 cryo-EM (orange and grey) and the Ca^{2+}-bound X-ray structure (dark grey and light blue, PDBID:
788 4WIS) The view is as in panel B. (**F**) View of the Ca^{2+}-ion binding site of the Ca^{2+}-bound state of
789 nhTMEM16 in DDM. Ca^{2+}-ions are displayed as blue spheres. (**G**) Cryo-EM map of the
790 nhTMEM16 dimer (green and grey) in DDM in the absence of Ca^{2+} at 3.7 Å sharpened with a b-
791 factor of –147 $Å^2$ and contoured at 6 σ. (**H**) Ribbon representation of a superposition the Ca^{2+}-
792 bound (orange and grey) and the Ca^{2+}-free structure (green and grey) in detergent determined by
793 cryo-EM. The view is as in panel B. (**I**) View of the Ca^{2+}-binding site in the Ca^{2+}-free state of
794 nhTMEM16 in DDM. The location of weak residual density at the center of the Ca^{2+}-binding site
795 is indicated in magenta. F,I The respective cryo-EM densities are contoured at 7 σ and shown as
796 mesh. The backbone is displayed as Cα-trace, selected side-chains as sticks.

797

798

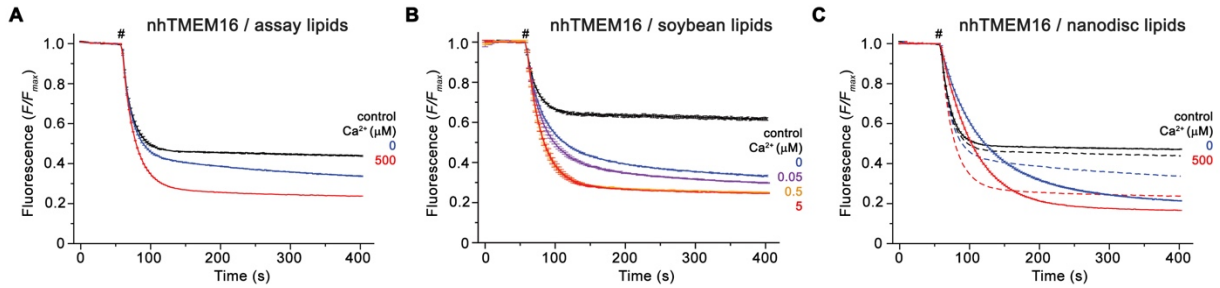

799

800 **Figure 1-figure supplement 1. Reconstitution of nhTMEM16 into liposomes.** Ca^{2+}-dependence
801 of scrambling activity of WT in liposomes of three different lipid compositions. Traces depict the
802 fluorescence decrease of tail-labeled NBD-PE lipids after addition of dithionite (#) at different
803 Ca^{2+} concentrations. Data show averages of three technical replicates for assay and nanodisc lipids,
804 and of two for soybean lipids. Ca^{2+} concentrations (μM) are indicated. (**A**) Scrambling activity of
805 nhTMEM16 reconstituted into liposomes composed of *E. coli* polar lipids, egg PC at a ratio of 3:1
806 (w/w) used for functional experiments. (**B**) Scrambling activity of nhTMEM16 reconstituted into
807 liposomes composed of soybean polar lipids extract with 20% cholesterol (w/w). (**C**) Scrambling
808 activity of nhTMEM16 reconstituted into liposomes composed of POPC/POPG at a molar ratio of
809 7:3 used for nanodisc assembly. Traces of *E. coli* polar lipids/egg PC-containing proteoliposomes
810 (displayed in A) are shown as dashed lines for comparison.

811

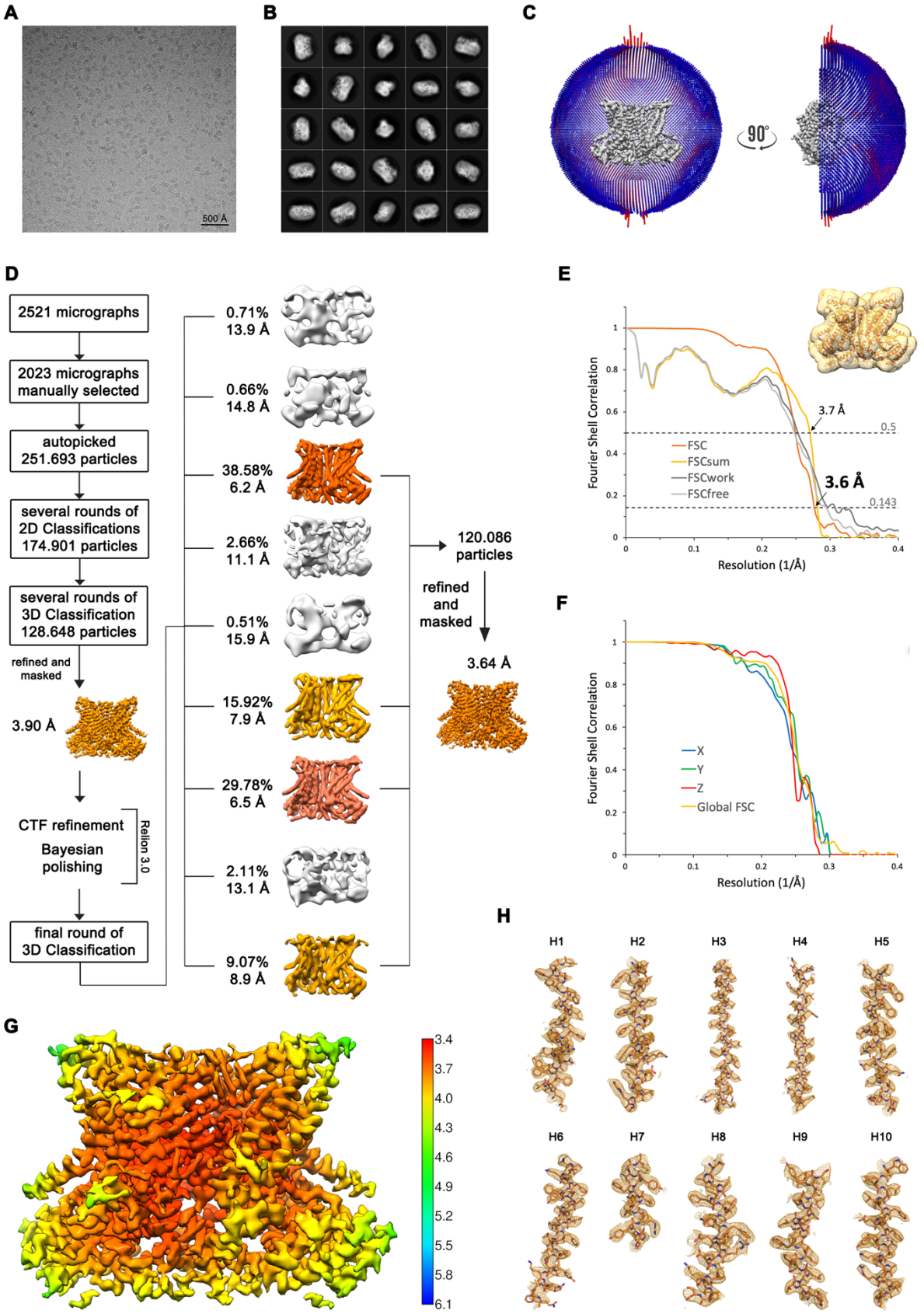
A
500 Å
B
C
90°
D
2521 micrographs
2023 micrographs manually selected
autopicked 251.693 particles
several rounds of 2D Classifications 174.901 particles
several rounds of 3D Classification 128.648 particles
refined and masked
3.90 Å
CTF refinement
Bayesian polishing
Relion 3.0
final round of 3D Classification
0.71% 13.9 Å
0.66% 14.8 Å
38.58% 6.2 Å
2.66% 11.1 Å
0.51% 15.9 Å
15.92% 7.9 Å
29.78% 6.5 Å
2.11% 13.1 Å
9.07% 8.9 Å
120.086 particles
refined and masked
3.64 Å
E
Fourier Shell Correlation
Resolution (1/Å)
FSC
FSCsum
FSCwork
FSCfree
3.7 Å
3.6 Å
0.5
0.143
F
Fourier Shell Correlation
Resolution (1/Å)
X
Y
Z
Global FSC
G
3.4
3.7
4.0
4.3
4.6
4.9
5.2
5.5
5.8
6.1
H
H1
H2
H3
H4
H5
H6
H7
H8
H9
H10

812

813 **Figure 1-figure supplement 2. Structure Determination of nhTMEM16 in DDM in complex**
814 **with Ca^{2+}.** (**A**) Representative cryo-EM image and (**B**) 2D-class averages of vitrified nhTMEM16
815 in a Ca^{2+}-bound state in detergent. (**C**) Angular distribution plot of particles included in the final
816 C2-symmetric 3D reconstruction. The number of particles with their respective orientation is
817 represented by length and color of the cylinders. (**D**) Image processing workflow. (**E**) FSC plot
818 used for resolution estimation and model validation. The gold-standard FSC plot between two
819 separately refined half-maps is shown in orange and indicates a final resolution of 3.6 Å. FSC
820 validation curves for FSCsum, FSCwork and FSCfree as described in the Methods are shown in
821 light yellow, dark grey and light grey, respectively. A thumbnail of the mask used for FSC
822 calculation overlaid on the atomic model is shown in the upper right corner and thresholds used
823 for FSCsum of 0.5 and for FSC of 0.143 are shown as dashed lines. (**F**) Anisotropy estimation plot
824 of the final map. The global FSC curve is represented in yellow. The directional FSCs along the
825 x, y and z axis displayed in blue, green and red, respectively, are indicative for an isotropic dataset.
826 (**G**) Final reconstruction map colored by local resolution as estimated by Relion, indicate regions
827 of higher resolution. (**H**) Sections of the cryo-EM density of the map superimposed on the refined
828 model. The model is shown as sticks and structural elements are labelled. The map was sharpened
829 with a b-factor of –126 $Å^2$ and contoured at 5 σ.
830

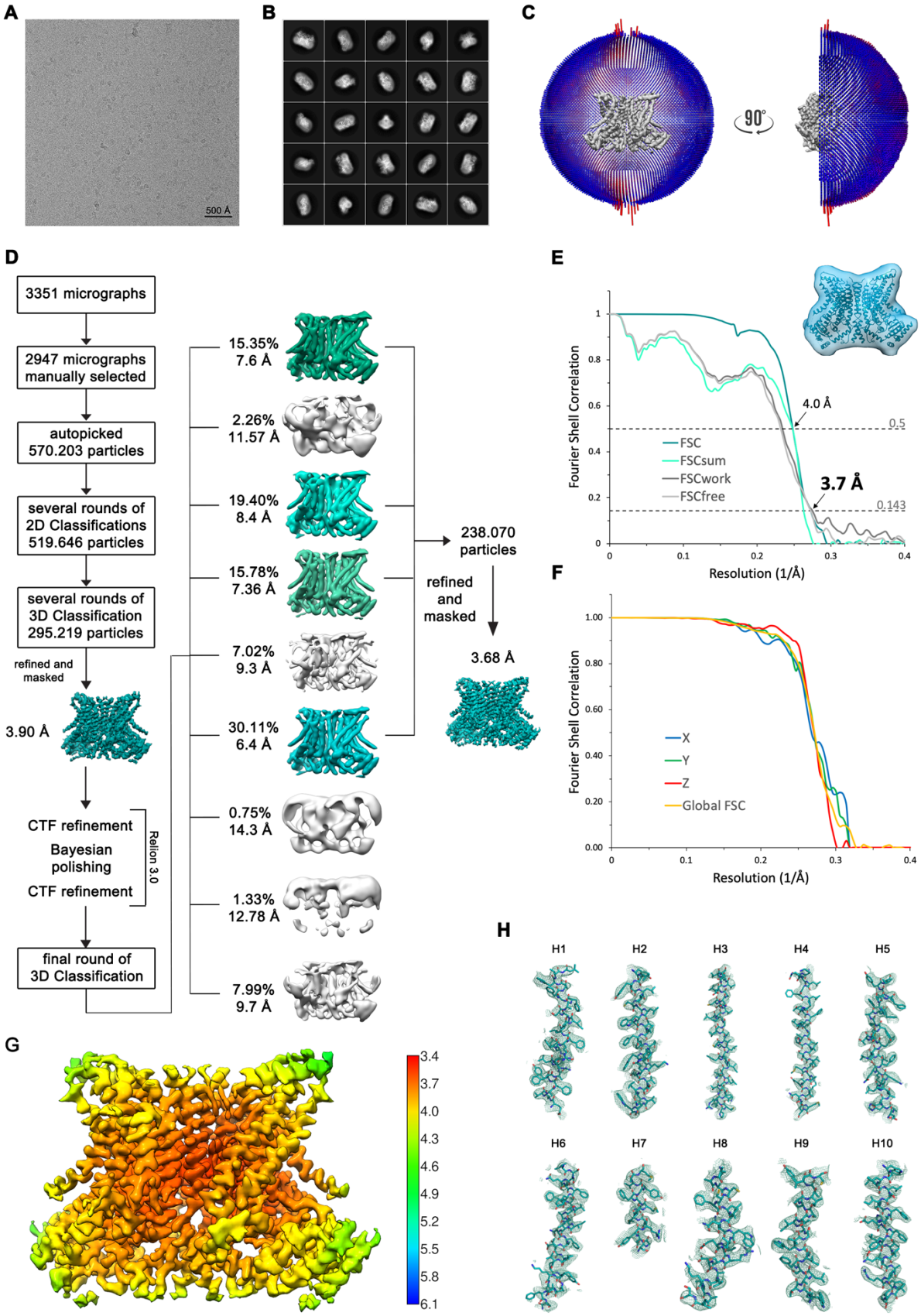
A
500 Å
B
C
90°
D
3351 micrographs
2947 micrographs manually selected
autopicked 570.203 particles
several rounds of 2D Classifications 519.646 particles
several rounds of 3D Classification 295.219 particles
refined and masked
3.90 Å
CTF refinement
Bayesian polishing
CTF refinement
Relion 3.0
final round of 3D Classification
15.35% 7.6 Å
2.26% 11.57 Å
19.40% 8.4 Å
15.78% 7.36 Å
7.02% 9.3 Å
30.11% 6.4 Å
0.75% 14.3 Å
1.33% 12.78 Å
7.99% 9.7 Å
238.070 particles
refined and masked
3.68 Å
E
Fourier Shell Correlation
Resolution (1/Å)
FSC
FSCsum
FSCwork
FSCfree
4.0 Å
3.7 Å
0.5
0.143
F
Fourier Shell Correlation
Resolution (1/Å)
X
Y
Z
Global FSC
G
3.4
3.7
4.0
4.3
4.6
4.9
5.2
5.5
5.8
6.1
H
H1
H2
H3
H4
H5
H6
H7
H8
H9
H10

831

832 **Figure 1-figure supplement 3. Structure Determination of nhTMEM16 in DDM in absence**
833 **of Ca^{2+}.** (**A**) Representative cryo-EM image and (**B**) 2D-class averages of vitrified nhTMEM16 in
834 a Ca^{2+}-free state in detergent. (**C**) Angular distribution plot of particles included in the final C2-
835 symmetric 3D reconstruction. The number of particles with their respective orientation is
836 represented by length and color of the cylinders. (**D**) Image processing workflow. (**E**) FSC plot
837 used for resolution estimation and model validation. The gold-standard FSC plot between two
838 separately refined half-maps is shown in green and indicates a final resolution of 3.7 Å. FSC
839 validation curves for FSCsum, FSCwork and FSCfree as described in the Methods are shown in
840 cyan, dark grey and light grey, respectively. A thumbnail of the mask used for FSC calculation
841 overlaid on the atomic model is shown in the upper right corner and thresholds used for FSCsum
842 of 0.5 and for FSC of 0.143 are shown as dashed lines. (**F**) Anisotropy estimation plot of the final
843 map. The global FSC curve is represented in yellow. The directional FSCs along the x, y and z
844 axis displayed in blue, green and red, respectively, are indicative for an isotropic dataset. (**G**) Final
845 reconstruction map colored by local resolution as estimated by Relion, indicate regions of higher
846 resolution. (**H**) Sections of the cryo-EM density of the map superimposed on the refined model.
847 The model is shown as sticks and structural elements are labelled. The map was sharpened with a
848 Fig1_S4b-factor of –147 $Å^2$ and contoured at 5 σ.
849

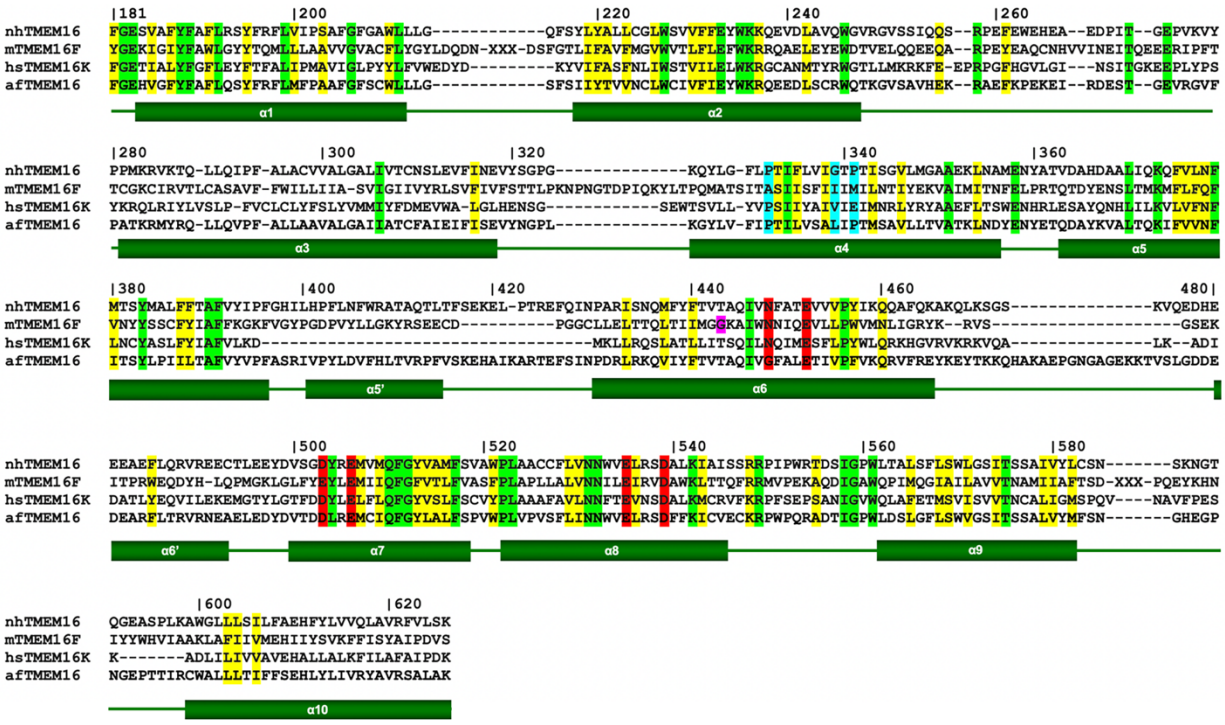

850

851 **Figure 1-figure supplement 4. Sequence alignment of selected TMEM16 scramblases.** Protein
852 sequences of the transmembrane domain of the fungal TMEM16 homologs from *Nectria*
853 *haematococca* (nhTMEM16) and *Aspergillus fumigatus* (afTMEM16), murine TMEM16F and
854 human TMEM16K were aligned based on their structure. Numbering and the boundaries of
855 secondary structure elements (green rectangles for transmembrane-helices and green lines for
856 loops) correspond to nhTMEM16. Residues highlighted in red constitute the Ca^{2+}-binding site;
857 residues highlighted in blue act as potential pivot points for structural arrangements in α4; residue
858 highlighted in purple indicates the flexible hinge region in TMEM16F responsible for the
859 movements of α6 upon Ca^{2+} release.

860

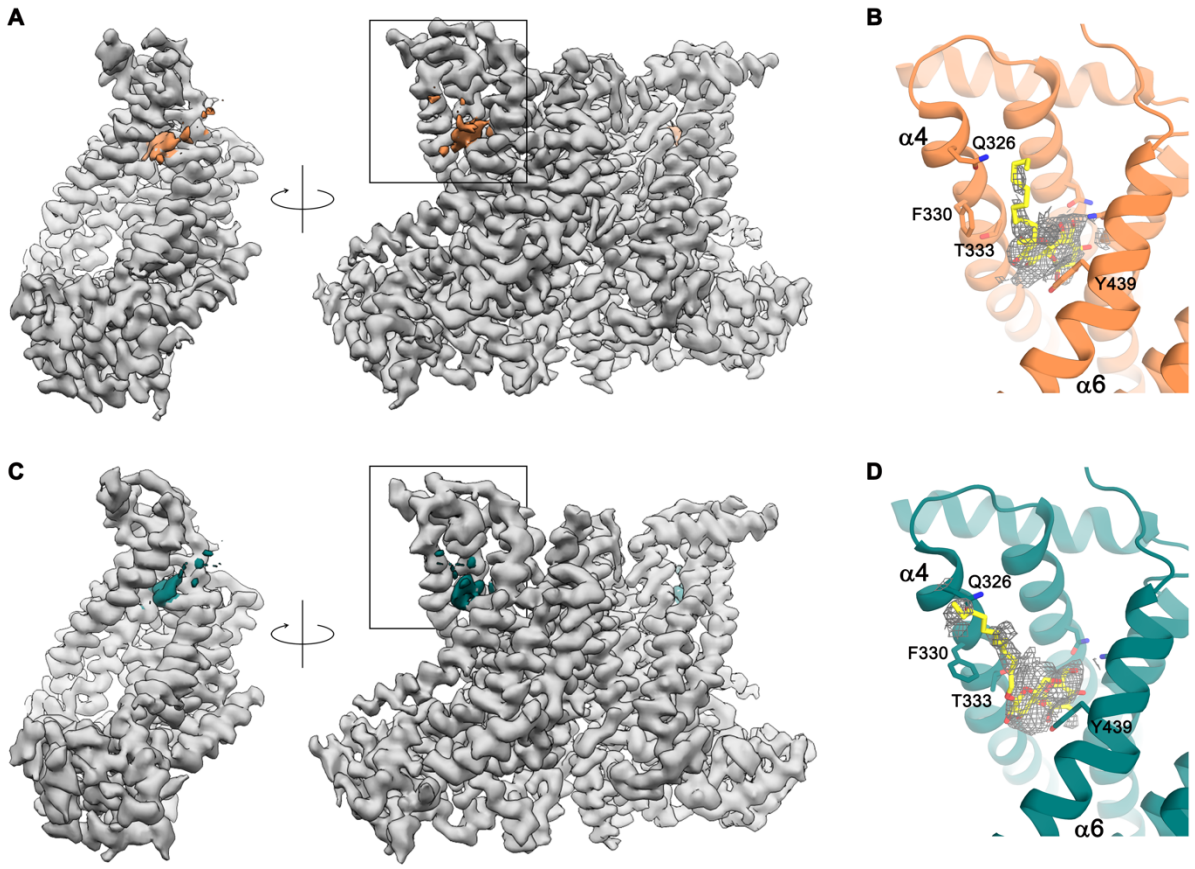

861

862 **Figure 1-figure supplement 5. Detergent binding to the subunit cavity.** (**A**) Cryo-EM map of
863 the nhTMEM16 dimer in detergents in presence of Ca^{2+} (grey) in two orientations. Residual
864 density in the subunit cavity highlighted in orange. (**B**) Ribbon representation of the subunit cavity
865 of nhTMEM16 in detergents in presence of Ca^{2+}. Residual density (contoured at 5 σ) is shown as
866 grey mesh. A DDM molecule (yellow) and selected sidechains are depicted as sticks. (**C**) Cryo-
867 EM map of the nhTMEM16 dimer in detergents in absence of Ca^{2+} (grey) in two orientations.
868 Residual density found in the subunit cavity is highlighted in green. (**D**) Ribbon representation of
869 the subunit cavity of nhTMEM16 in detergents in absence of Ca^{2+} (green). Residual density
870 (contoured at 5 σ) is shown as grey mesh. A DDM molecule (yellow) is depicted as sticks. The
871 location of B,D is indicated by the box drawn on the right panel of A,C.

872

873

874

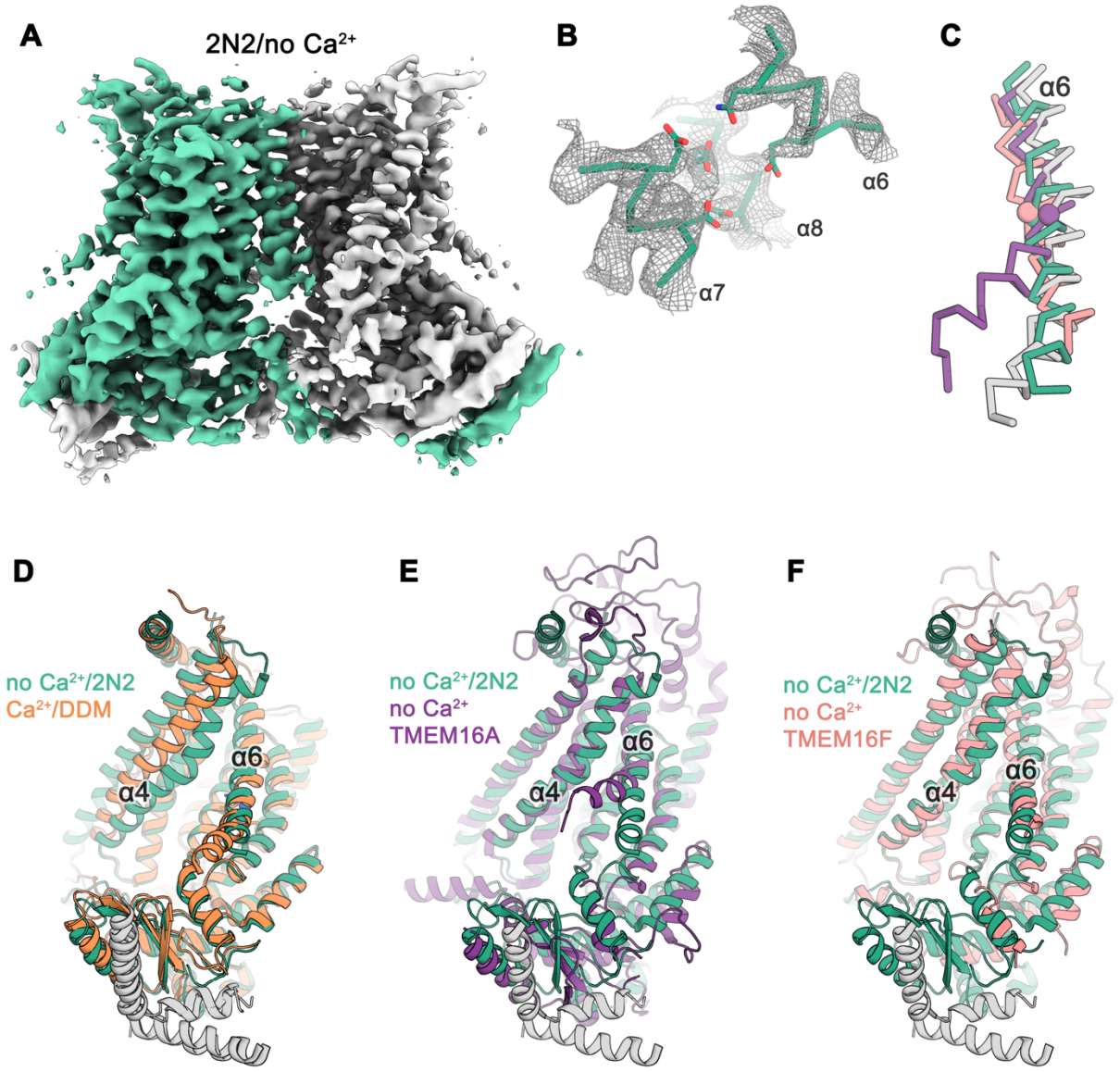

875

876 **Figure 2. Cryo-EM structure of nhTMEM16 in nanodiscs in absence of Ca^{2+}.** (**A**) Cryo-EM
877 map of the nhTMEM16 dimer (light green and grey) in nanodiscs in absence of Ca^{2+} at 3.8 Å
878 resolution. The map was sharpened with a b-factor of –150 $Å^2$ and is contoured at 5.6 σ. (**B**) View
879 of the Ca^{2+}-binding site in the Ca^{2+}-free state of nhTMEM16 in nanodiscs. The cryo-EM density

880 shown as mesh is contoured at 6 σ, the backbone is displayed as Cα-trace and selected side-chains
881 as sticks. (**C**) Cα-traces of α6 from a superposition of Ca^{2+}-free structures of nhTMEM16 in
882 nanodiscs (green), TMEM16A (violet, PDBID: 5OYG) and TMEM16F (red) and of the Ca^{2+}-
883 bound structure of nhTMEM16 in DDM (grey). The spheres indicate the position of the flexible
884 glycine residue in TMEM16A and TMEM16F, which acts as a hinge for conformational changes.
885 (**D-F**) Ribbon representation of superpositions of the Ca^{2+}-free structure in nanodiscs (light green
886 and grey) and the Ca^{2+}-bound structure in DDM (**D**, orange and grey), the Ca^{2+}-free structure of
887 TMEM16A (**E**, violet, PDBID: 5OYG), the Ca^{2+}-free structure of TMEM16F (**F**, red). Selected
888 α-helices are labeled, the views are as in Figure 1.

889

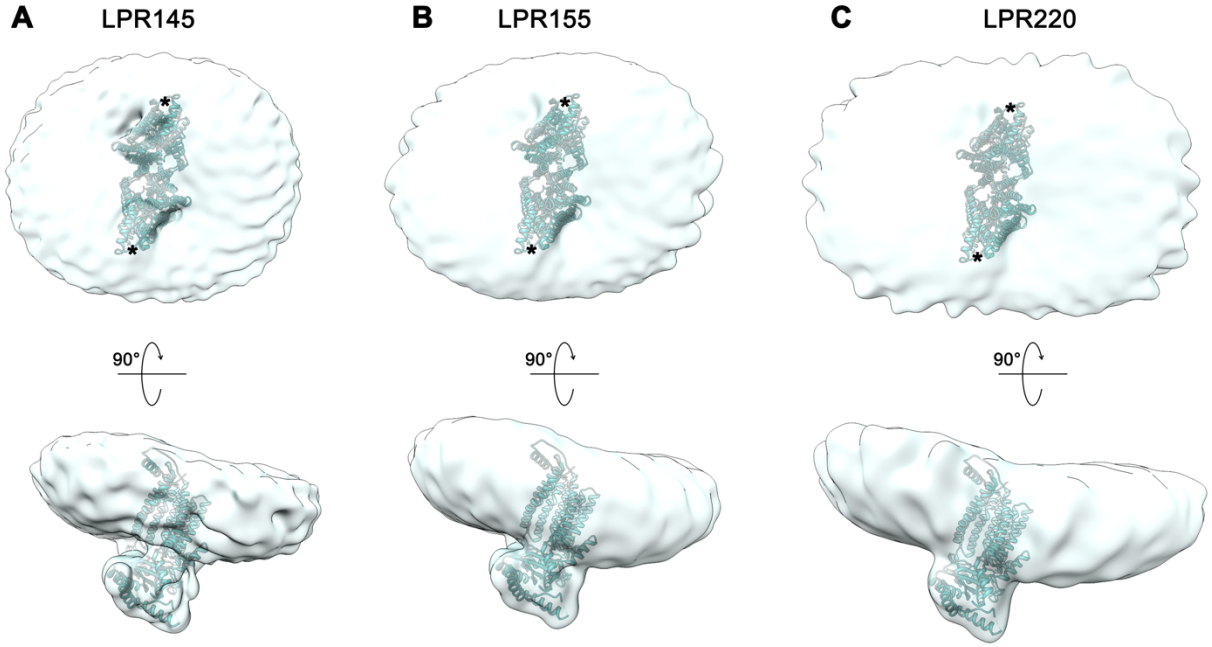

890

891 **Figure 2-figure supplement 1. Reconstitution of nhTMEM16 into nanodiscs.** Shape of
892 nhTMEM16 particles reconstituted into nanodiscs at different protein to lipid ratios (LPR,
893 mol/mol) in the absence of Ca^{2+}: (**A**), LPR 145, (**B**), LPR 155 and(**C**), LPR 220. Refined and

894 unmasked cryo-EM density maps were low-pass filtered to 10 Å and are shown from the
895 extracellular side (upper panel, subunit cavity indicated by *) and from the side with a view
896 towards the subunit cavity (lower panel). A model of nhTMEM16 fitted into the density is
897 displayed as ribbon.
898
899

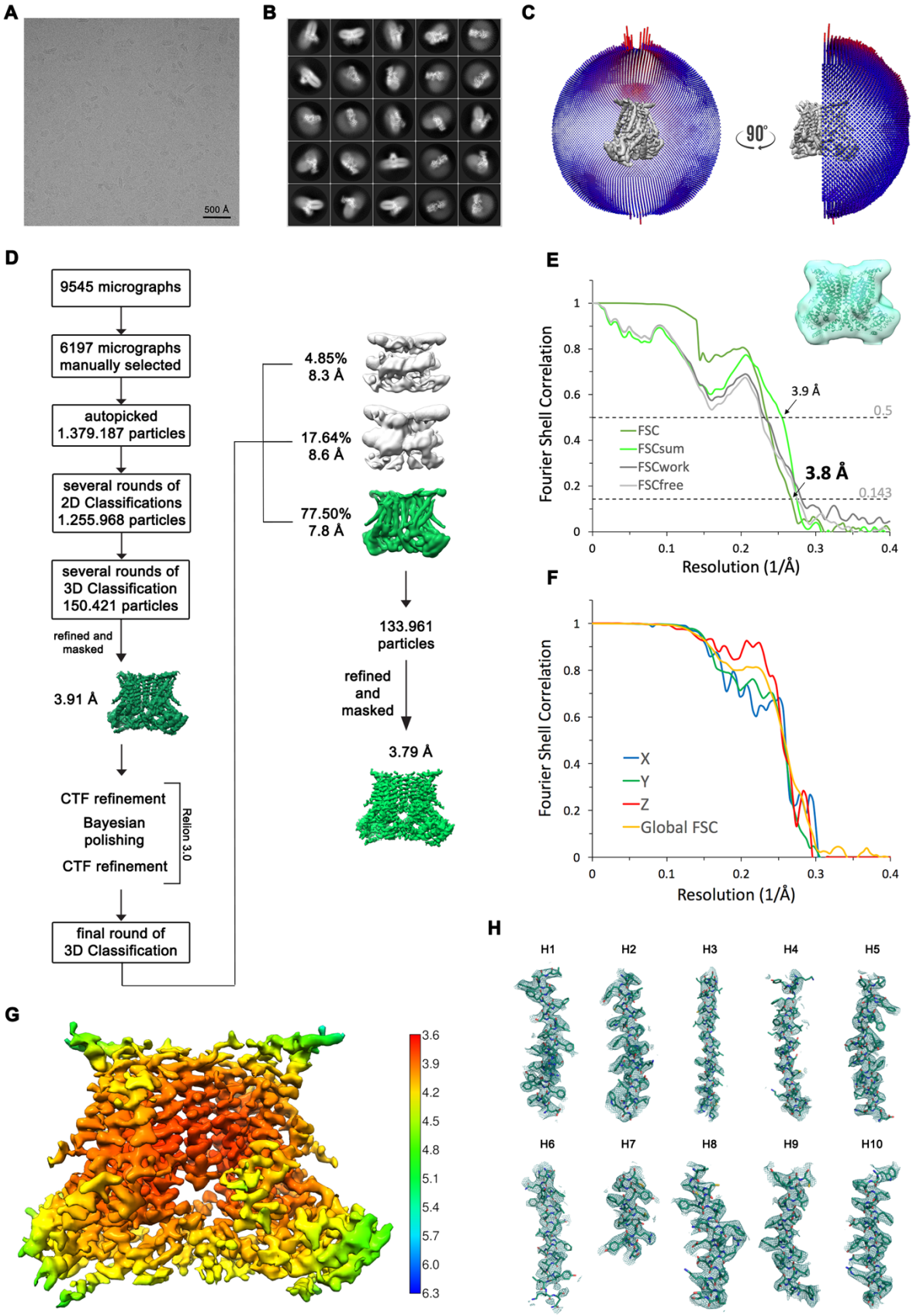
A
500 Å
B
C
90°
D
9545 micrographs
6197 micrographs manually selected
autopicked 1.379.187 particles
several rounds of 2D Classifications 1.255.968 particles
several rounds of 3D Classification 150.421 particles
refined and masked
3.91 Å
CTF refinement
Bayesian polishing
CTF refinement
Relion 3.0
final round of 3D Classification
4.85% 8.3 Å
17.64% 8.6 Å
77.50% 7.8 Å
133.961 particles
refined and masked
3.79 Å
E
Fourier Shell Correlation
Resolution (1/Å)
FSC
FSCsum
FSCwork
FSCfree
3.9 Å
3.8 Å
0.5
0.143
F
Fourier Shell Correlation
Resolution (1/Å)
X
Y
Z
Global FSC
G
3.6
3.9
4.2
4.5
4.8
5.1
5.4
5.7
6.0
6.3
H
H1
H2
H3
H4
H5
H6
H7
H8
H9
H10

900

901 **Figure 2-figure supplement 2. Structure Determination of nhTMEM16 in the absence of Ca^{2+}**
902 **in nanodiscs.** (**A**) Representative cryo-EM image and (**B**) 2D-class averages of vitrified
903 nhTMEM16 in a Ca^{2+}-free state in lipid nanodiscs. (**C**) Angular distribution plot of particles
904 included in the final C2-symmetric 3D reconstruction. The number of particles with their
905 respective orientation is represented by length and color of the cylinders. (**D**) Image processing
906 workflow. (**E**) FSC plot used for resolution estimation and model validation. The gold-standard
907 FSC plot between two separately refined half-maps is shown in green and indicates a final
908 resolution of 3.8 Å. FSC validation curves for FSCsum, FSCwork and FSCfree as described in the
909 Methods are shown in light green, dark grey and light grey, respectively. A thumbnail of the mask
910 used for FSC calculation overlaid on the atomic model is shown in the upper right corner and
911 thresholds used for FSCsum of 0.5 and for FSC of 0.143 are shown as dashed lines. (**F**) Anisotropy
912 estimation plot of the final map. The global FSC curve is represented in yellow. The directional
913 FSCs along the x, y and z axis displayed in blue, green and red, respectively, are indicative for an
914 isotropic dataset. (**G**) Final reconstruction map colored by local resolution as estimated by Relion,
915 indicate regions of higher resolution. (**H**) Sections of the cryo-EM density of the map
916 superimposed on the refined model. The model is shown as sticks and structural elements are
917 labelled. The map was sharpened with a b-factor of –150 $Å^2$ and contoured at 5 σ.
918

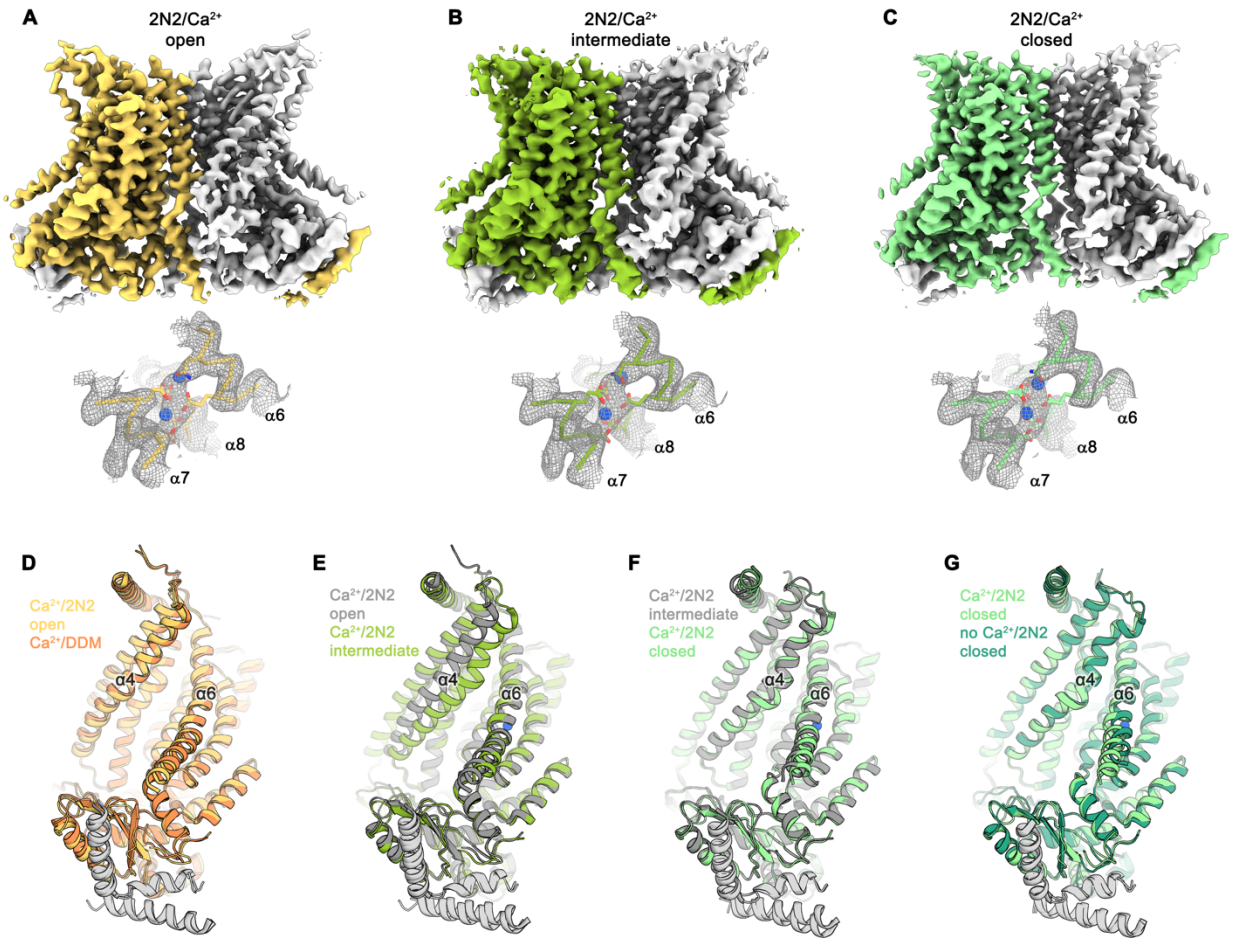

Figure 3. Cryo-EM structures of nhTMEM16 in nanodiscs in presence of Ca^{2+}. (**A**) Cryo-EM map of the nhTMEM16 dimer in the Ca^{2+}-bound 'open' state (yellow and grey) in nanodiscs at 3.6 Å sharpened with a b-factor of –114 $Å^2$ and contoured at 6.5 σ (upper panel). Close-up of the Ca^{2+}-binding site with two bound Ca^{2+}-ions displayed as blue spheres (lower panel). Cryo-EM density contoured at 7 σ is shown as grey mesh, the backbone is displayed as yellow Cα-trace, selected side-chains as sticks. (**B**) Cryo-EM map of the nhTMEM16 dimer in the Ca^{2+}-bound 'intermediate' state (yellow-green and grey) in nanodiscs at 3.7 Å sharpened with a b-factor of –96 $Å^2$ and contoured at 4.9 σ (upper panel). Close-up of the Ca^{2+}-binding site with two bound Ca^{2+}-ions displayed as blue spheres (lower panel). Cryo-EM density contoured at 7 σ is shown as grey mesh, the backbone is displayed as light green Cα-trace, selected side-chains as sticks. (**C**) Cryo-

930 EM map of the nhTMEM16 dimer in the ‘Ca^{2+}-bound closed state (green and grey) in nanodiscs
931 at 3.6 Å sharpened with a b-factor of –96 $Å^2$ and contoured at 6.5 σ (upper panel). Close-up of the
932 Ca^{2+}-binding site with two bound Ca^{2+}-ions displayed as blue spheres (lower panel). Cryo-EM
933 density contoured at 7 σ is shown as grey mesh, the backbone is displayed as light green Cα-trace,
934 selected side-chains as sticks. (**D-G**) Ribbon representation of superpositions with Ca^{2+}-bound
935 structures of nhTMEM16 in nanodiscs: (**D**) Ca^{2+}-bound open structure in nanodiscs and Ca^{2+}-
936 bound structure in DDM; (**E**) Ca^{2+}-bound open structure in nanodiscs and Ca^{2+}-bound intermediate
937 structure in nanodiscs; (**F**) Ca^{2+}-bound intermediate structure in nanodiscs and Ca^{2+}-bound closed
938 structure in nanodiscs; (**G**) Ca^{2+}-bound closed structure in nanodiscs and Ca^{2+}-free structure in
939 nanodiscs. Selected helices are labeled and views are as in Figure 1.

940

941

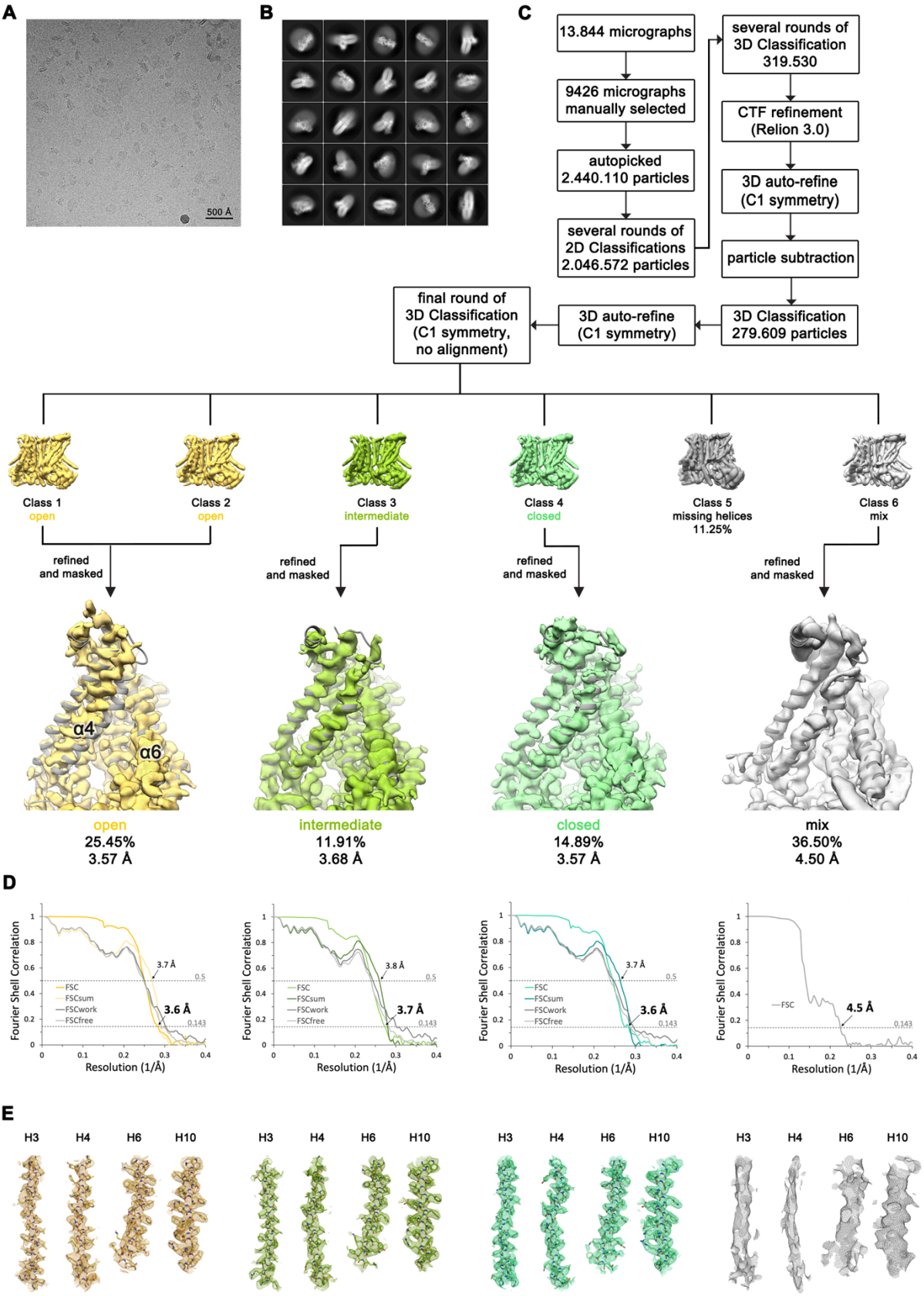
A
500 Å
B
C
13.844 micrographs
9426 micrographs manually selected
autopicked 2.440.110 particles
several rounds of 2D Classifications 2.046.572 particles
several rounds of 3D Classification 319.530
CTF refinement (Relion 3.0)
3D auto-refine (C1 symmetry)
particle subtraction
3D Classification 279.609 particles
3D auto-refine (C1 symmetry)
final round of 3D Classification (C1 symmetry, no alignment)
Class 1 open
Class 2 open
Class 3 intermediate
Class 4 closed
Class 5 missing helices 11.25%
Class 6 mix
refined and masked
α4
α6
open 25.45% 3.57 Å
intermediate 11.91% 3.68 Å
closed 14.89% 3.57 Å
mix 36.50% 4.50 Å
D
Fourier Shell Correlation
Resolution (1/Å)
FSC
FSCsum
FSCwork
FSCfree
3.7 Å
3.6 Å
3.8 Å
4.5 Å
0.5
0.143
E
H3
H4
H6
H10

942

943 **Figure 3-figure supplement 1. Structure Determination of nhTMEM16 in complex with Ca^{2+}**
944 **in nanodiscs.** (**A**) Representative cryo-EM image and (**B**) 2D-class averages of vitrified
945 nhTMEM16 in a Ca^{2+}-bound state in lipid nanodiscs. (**C**) Image processing workflow. The final
946 set of subtracted particles was subjected to a final round of 3D classification disclosing a
947 conformational heterogeneity at the subunit cavity, with classes resembling a well-resolved open,
948 intermediate and closed state of the subunit cavity. Other classes displayed a poorly resolved
949 density for α3 and α4 that likely represents an average of several transition states. Close-up of the
950 subunit cavity show the intermediate model (grey) superimposed on the cryo-EM maps of the
951 respective classes. View as in Figure 3C-F. (**D**) FSC plot used for resolution estimation and model
952 validation for each state. The gold-standard FSC plot between two separately refined half-maps is
953 shown in yellow. FSC validation curves for FSCsum, FSCwork and FSCfree as described in the
954 Methods are shown in light yellow, dark grey and light grey, respectively. Thresholds used for
955 FSCsum of 0.5 and for FSC of 0.143 are shown as dashed lines. (**E**) Sections of the cryo-EM
956 density of the maps superimposed on the corresponding refined models. The models are shown as
957 sticks and structural elements are labelled. The maps were contoured at 4.5 σ.
958

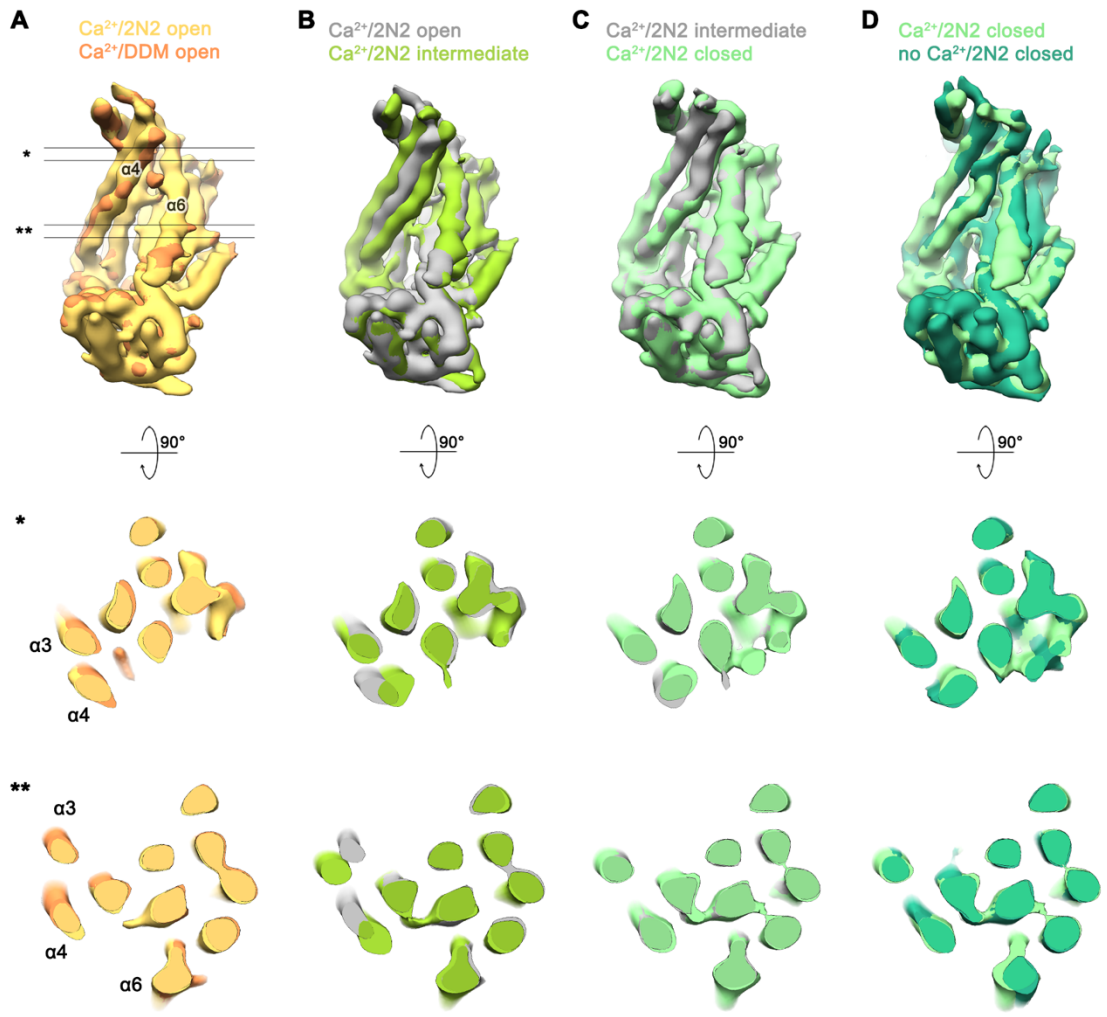

959

960 **Figure 3-figure supplement 2. Conformational heterogeneity in the Ca^{2+}-bound data of**
961 **nhTMEM16 in nanodiscs. (A-D)** Superpositions of the refined and unmasked cryo-EM maps of
962 Ca^{2+}-bound structures of nhTMEM16 in nanodiscs, low-pass filtered at 6 Å. (**A**) Superposition of
963 the Ca^{2+}-bound open structure in nanodiscs and the Ca^{2+}-bound structure in DDM; (**B**) the Ca^{2+}-
964 bound open structure in nanodiscs and the Ca^{2+}-bound intermediate structure in nanodiscs; (**C**) the
965 Ca^{2+}-bound intermediate structure in nanodiscs and the Ca^{2+}-bound closed structure in nanodiscs;
966 (**D**) the Ca^{2+}-bound closed structure in nanodiscs and the Ca^{2+}-free structure in nanodiscs. A-D,
967 selected helices are labeled, view of upper panel is as in Figure 3C-F. Middle and lower panel

968 show a cross-section through the superposition at the indicated positions indicated in A by * and

969 **.

970

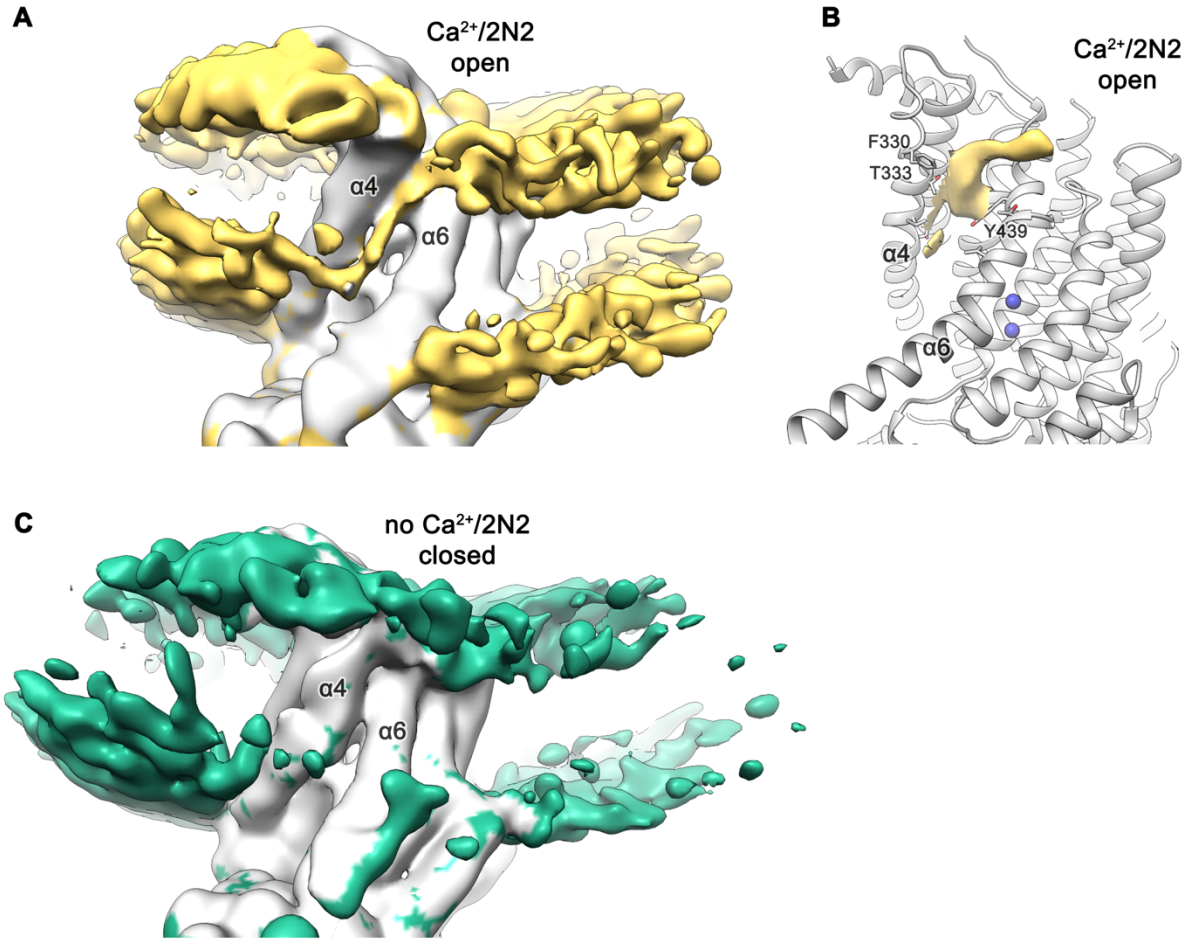

971

972 **Figure 3-figure supplement 3. Lipid distribution at the subunit cavity.** (**A**) Cryo-EM map of

973 Ca^{2+}-bound nhTMEM16 in nanodiscs (grey, contoured at 3.4 σ) with density corresponding to the

974 phospholipid headgroup region of both membrane leaflets in the nanodisc and inside the subunit

975 cavity highlighted in yellow. (**B**) Ribbon representation of the subunit cavity of the Ca^{2+}-bound

976 nhTMEM16 in nanodiscs (grey) with selected sidechains labelled and depicted as sticks.

977 Unassigned density inside the subunit cavity (contoured at 3.9 σ) is shown in yellow. (**C**) Cryo-

978 EM map of Ca^{2+}-free nhTMEM16 in nanodiscs (grey, contoured at 3.4 σ) with density of the

979 phospholipid headgroup region of both membrane leaflets in the nanodisc highlighted in green.
980 No residual density is found at the subunit cavity. A,C The refined and unmasked maps were low-
981 pass filtered to 6 Å.
982

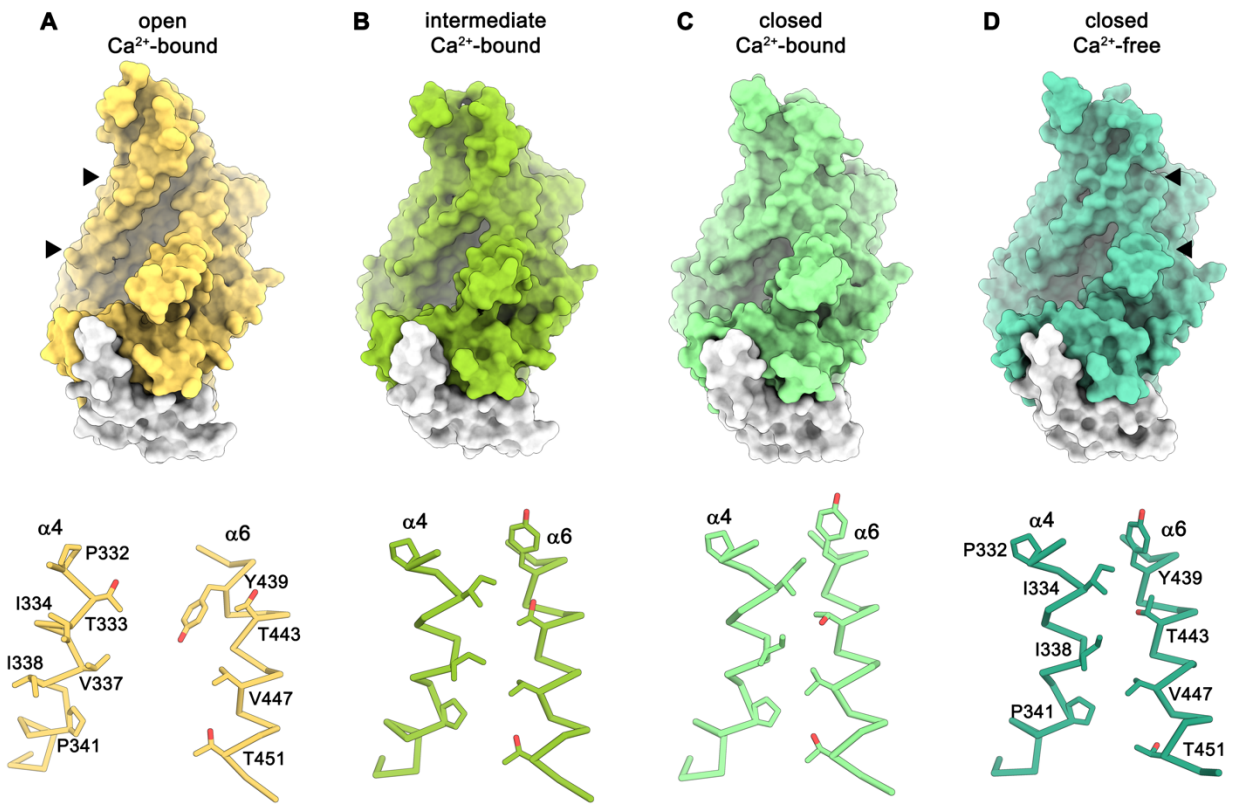

983

984 **Figure 4. Conformations of the 'subunit cavity'.** Views of the molecular surface of the subunit
985 cavity (top) and structures of α4 and α6 that line the cavity displayed as Cα-trace with selected
986 sidechains shown as sticks and labeled (bottom). (**A**) 'Open state' as defined in the Ca^{2+}-bound
987 structure in nanodiscs. (**B**) 'Intermediate state' as defined in the Ca^{2+}-bound structure in nanodiscs,
988 (**C**) 'Ca^{2+}-bound closed state' as defined in the Ca^{2+}-bound structure in nanodiscs. (**D**) 'Closed
989 state' as defined by the Ca^{2+}-free structure in nanodiscs. The region shown in the lower panels is
990 depicted by triangles in the upper panels.

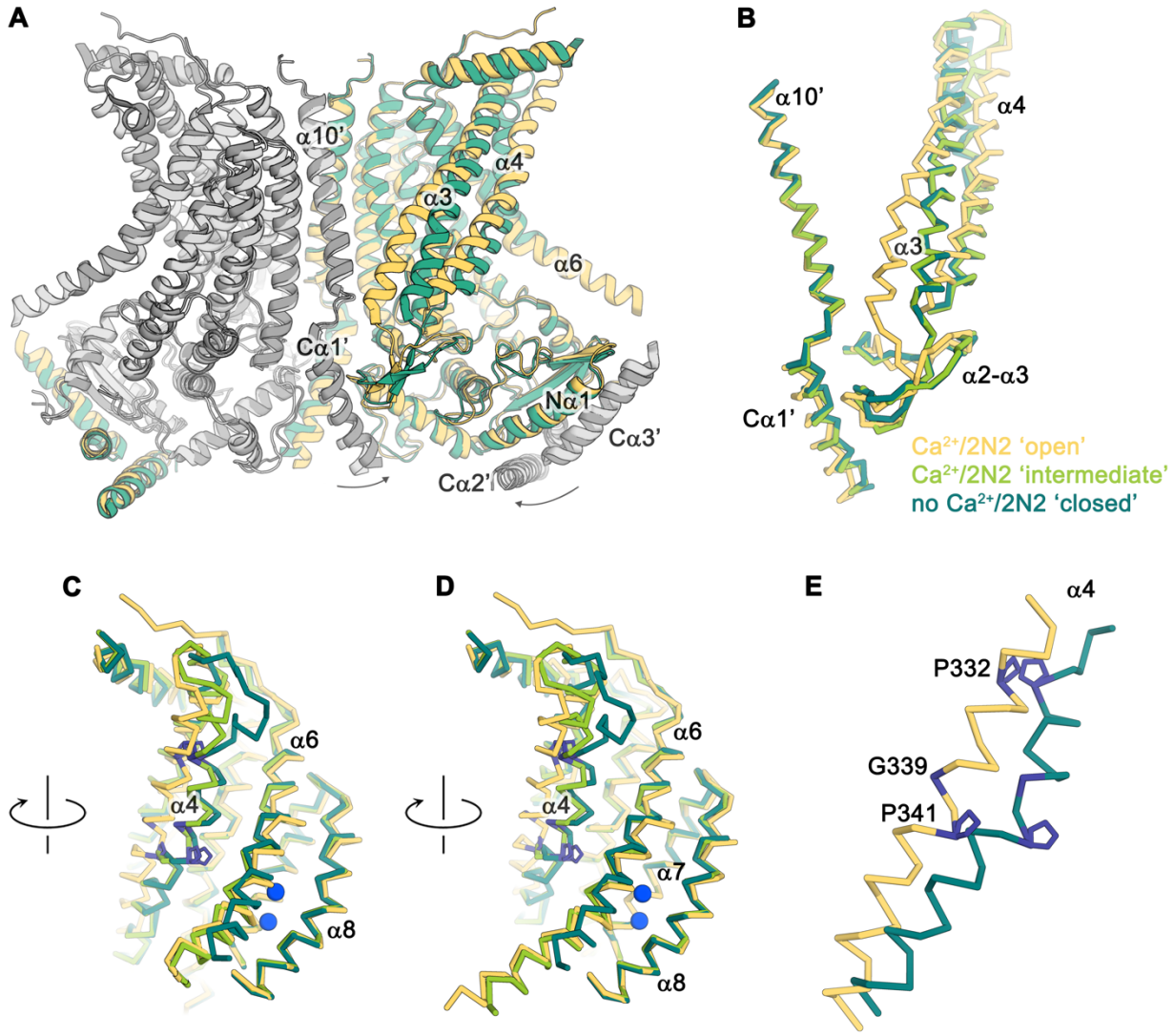

991

992 **Figure 5. Conformational changes.** (**A**) Ribbon representation of a superposition of the Ca^{2+}-
993 bound 'open' (yellow and light grey) and Ca^{2+}-free 'closed' (green and dark grey) nhTMEM16
994 structures in nanodiscs. Selective helices are labeled and the arrows indicate small rearrangements
995 of the cytosolic domain upon Ca^{2+}-release. (**B-D**) Cα-traces of selected regions of the 'subunit
996 cavity' in different conformations as defined by the Ca^{2+}-bound 'open' structure in nanodiscs
997 (yellow), the Ca^{2+}-bound 'intermediate' structure in nanodiscs (light green) and the Ca^{2+}-free
998 'closed' structure in nanodiscs (dark green). The view in B is as in A and the respective orientations

999 of subsequent panels are indicated. (**D**) Superposition of α4 in the 'open' and closed' states with

1000 residues that act as potential pivots for structural arrangements highlighted in blue.

1001

1002

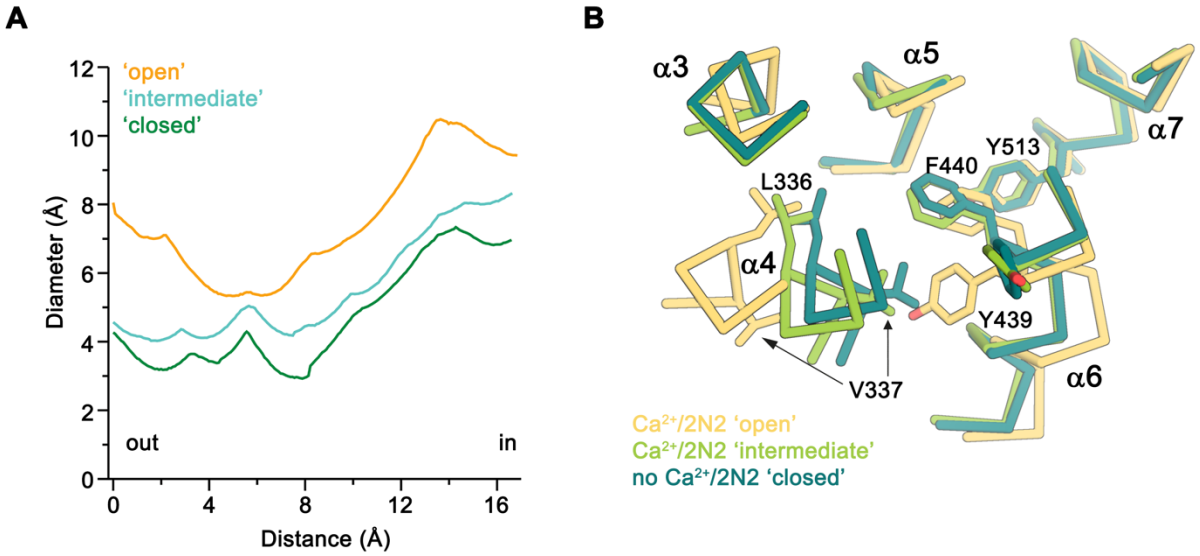

1003

1004 **Figure 5-figure supplement 1. Diameter of the subunit cavity in Ca^{2+}-bound nhTMEM16**

1005 **structures in nanodiscs.** (**A**) Pore diameter at the constriction of the subunit cavity in the three

1006 conformations of the subunit cavity calculated with HOLE (Smart et al., 1996). (**B**) View of the

1007 constriction of the 'subunit cavity' in three different conformations from the extracellular side.

1008 The protein is shown as Cα-trace with selected sidechains displayed as sticks and labelled.

1009

1010

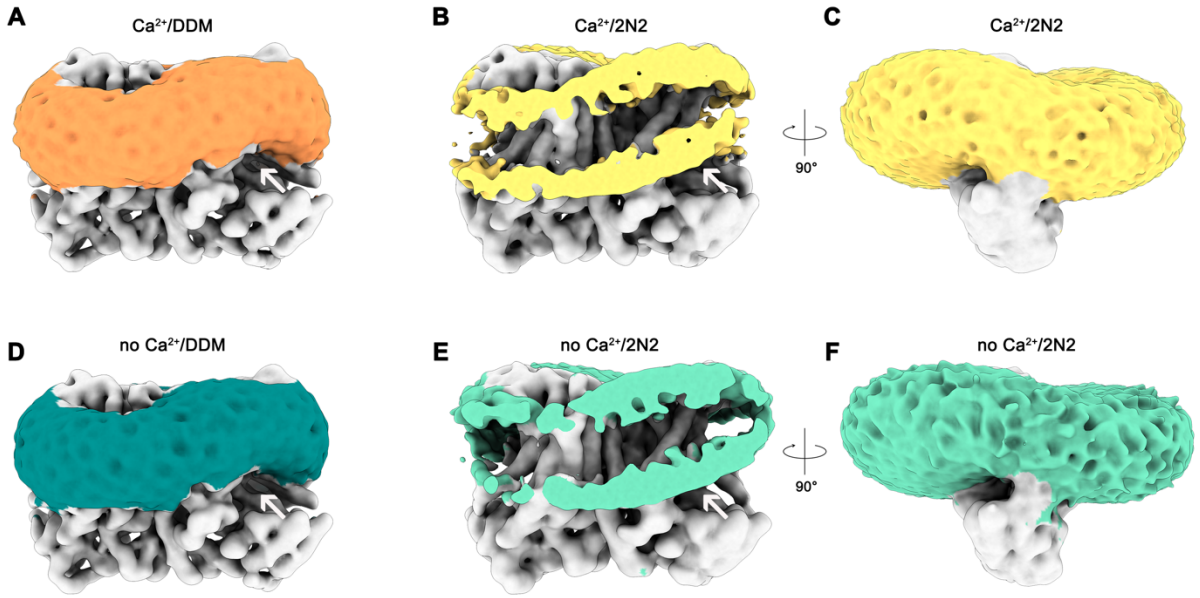

Figure 6. Detergent and lipid interactions. Refined and unmasked cryo-EM density map low-pass filtered to 6 Å are shown. (**A**) Map of the Ca^{2+}-bound nhTMEM16 data in detergent contoured at 4 σ ; (**B**,**C**) Map of the Ca^{2+}-bound nhTMEM16 data in nanodiscs contoured at 3.2 and 1.6 σ; (**D**) Map of the Ca^{2+}-free nhTMEM16 data in detergent contoured at 4 σ; (**E** and **F**), Map of the Ca^{2+}-free nhTMEM16 data in nanodiscs contoured at 3.2 and 1.6 σ. The density corresponding to the detergent micelle or the nanodisc, which is composed of lipids surrounded by the 2N2 belt protein, are colored in orange, yellow, dark green and light green, respectively, density of nhTMEM16 is shown in grey. A,B,D,E show a front view of the dimer similar to Figure 1A and the subunit cavity is indicated by a white arrow. B, E, clipped maps reveal the headgroup regions of both membrane leaflets. C,F, are viewed in direction of the subunit cavity.

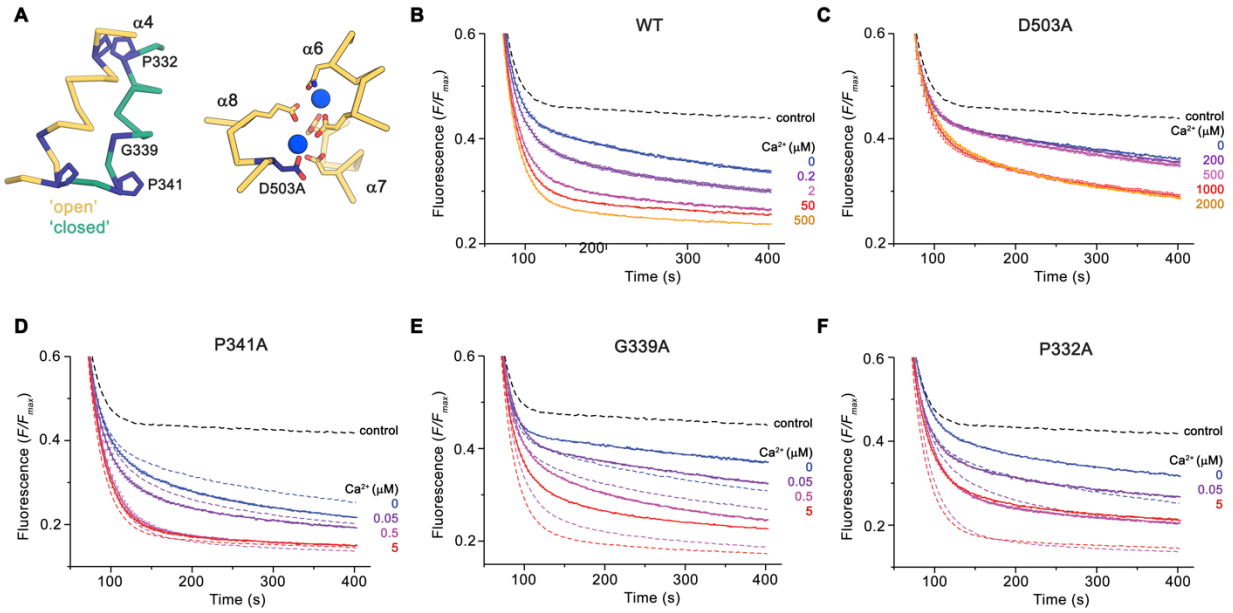

1023

1024 **Figure 7. Functional properties of mutants.** (**A**) Regions of nhTMEM16 harboring mutated
1025 residues. Left, Cα-trace of α4 in 'open' (yellow) and 'closed' (green) conformations of Ca^{2+}-bound
1026 nhTMEM16 in nanodiscs. Right, ion binding site with Ca^{2+}-ions shown in blue. (**B-F**) Ca^{2+}-
1027 dependence of scrambling activity in nhTMEM16-containing proteoliposomes. Traces depict
1028 sections of the fluorescence decrease of tail-labeled NBD-PE lipids after addition of dithionite at
1029 different Ca^{2+} concentrations. Data show averages of three technical replicates, errors are s.e.m..
1030 Ca^{2+} concentrations (μM) are indicated. Full traces are displayed in Fig7-figure supplement 1. (B)
1031 WT, (C) D503A, (D) P341A, (E) G339A, and (F) P332A. (D to F) The traces of WT reconstituted
1032 in the same batch of liposomes are shown as dashed lines in the same color as their corresponding
1033 conditions of the mutant for comparison. (B to F), The black dashed line refers to the fluorescence
1034 decay in protein-free liposomes.

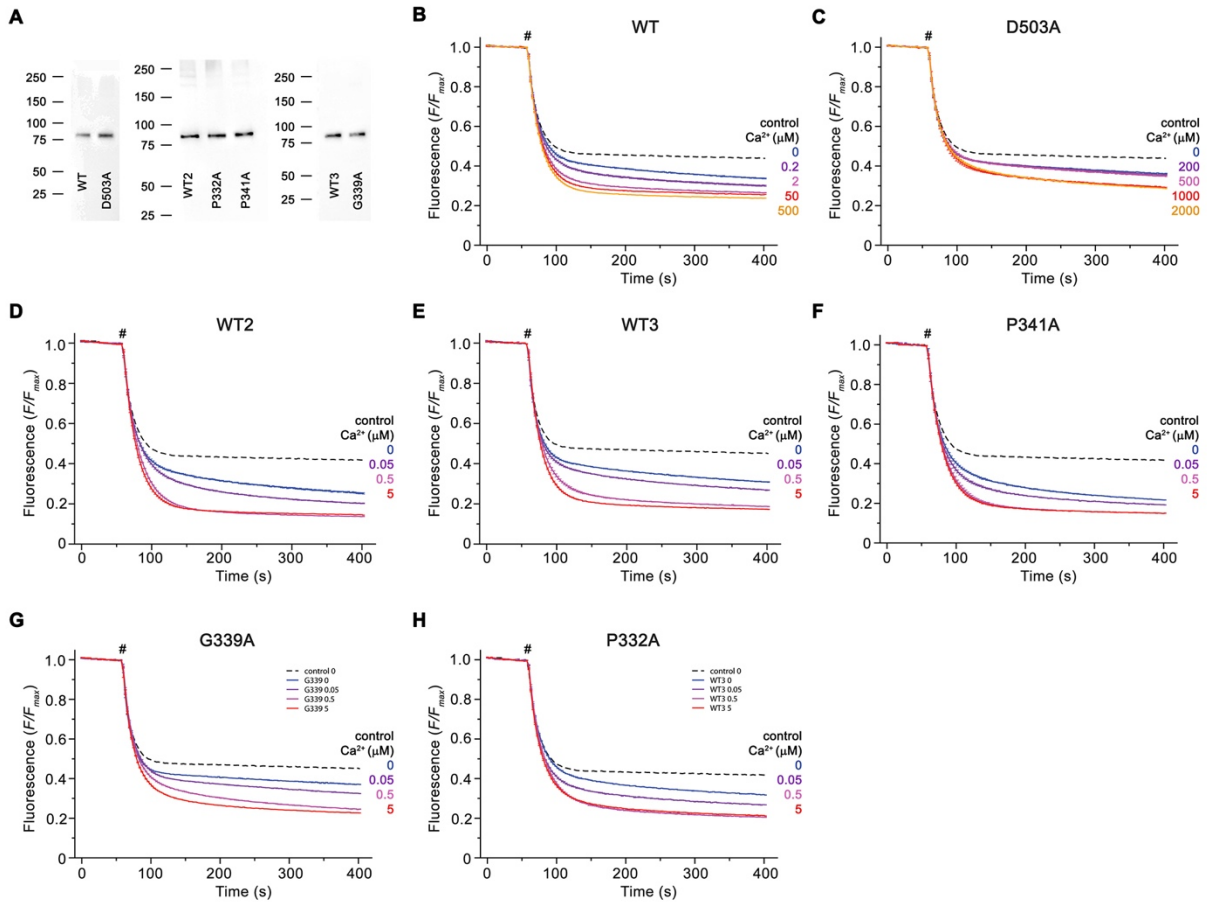

1035

1036 **Figure 7-figure supplement 1. Reconstitution efficiency.** (**A**) Reconstitution efficiency of
1037 nhTMEM16 mutants compared to WT (WT1, WT2, WT3) reconstituted in the same batch of
1038 solubilized lipids. For analysis, equivalent amounts of liposomes were loaded on SDS-PAGE and
1039 detected with an anti-my antibody detecting a fusion tag on the protein. The positions of molecular
1040 weight markers (kDa) are indicated. (**B-H**) Traces of scrambling experiments displayed in Figure
1041 7. Data show averages of three technical replicates, errors are s.e.m.. Ca^{2+}-dependence of
1042 scrambling activity of WT1 (**B**) and D503A (**C**) displayed in Figure 7B and C. (**D**) Ca^{2+}-
1043 dependence of scrambling activity of WT2 displayed for comparison in Figures 7D and F. (**E**)
1044 Ca^{2+}-dependence of scrambling activity of WT3 displayed for comparison in Figure 7E. (**F**) Ca^{2+}-
1045 dependence of scrambling activity of P341A displayed for comparison in Figure 7D. (**G**) Ca^{2+}-

1046 dependence of scrambling activity of G339A displayed for comparison in Figure 7E. (**H**) Ca^{2+}-
1047 dependence of scrambling activity of P332A displayed for comparison in Figure 7F. Traces depict
1048 fluorescence decrease of tail-labeled NBD-PE lipids after addition of dithionite (#) at different
1049 Ca^{2+} concentrations. Data show averages of three technical replicates. Ca^{2+} concentrations (μM)
1050 are indicated.
1051

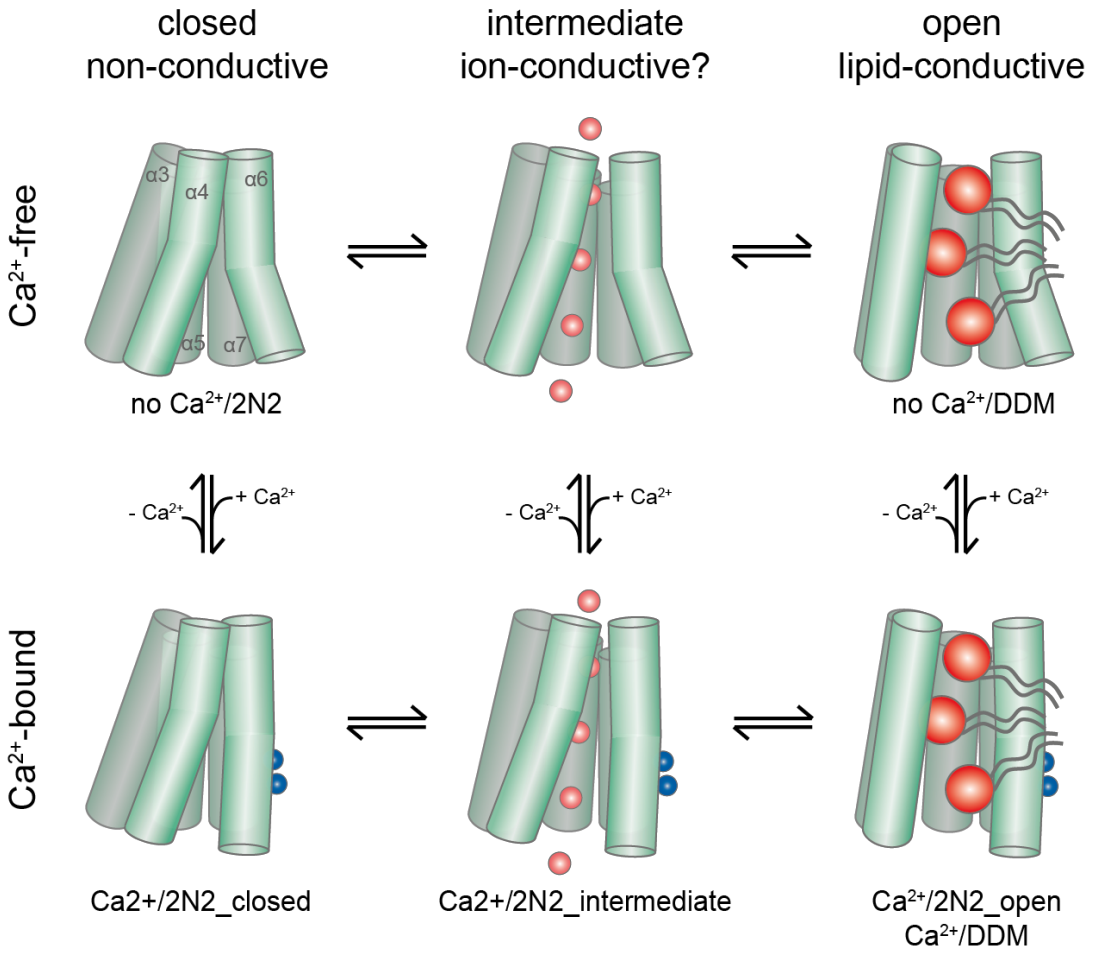

1052

1053 **Figure 8. Activation mechanism.** Scheme of the stepwise activation of nhTMEM16 displaying
1054 the equilibrium of states in Ca^{2+}-bound and Ca^{2+}-free conditions. Conformations obtained in this
1055 study and their correspondence to distinct states are indicated. Ca^{2+} and permeating ions are

1056 depicted as blue and red spheres, respectively. Phospholipid headgroups are shown as red spheres

1057 and acyl chains as grey tails.

1058

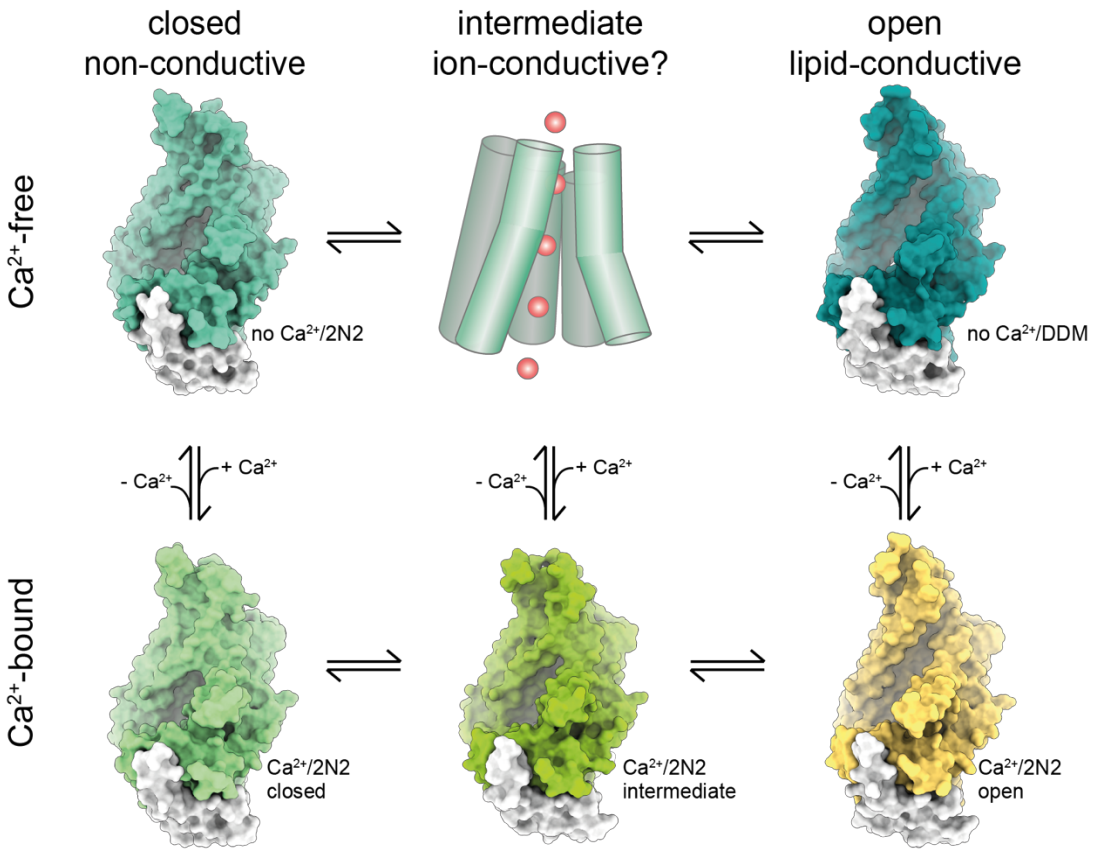

1059

1060 **Figure 8-figure supplement 1. Activation mechanism.** Scheme of the stepwise activation of

1061 nhTMEM16 as shown in Figure 8 with the states displayed by the surface representation of the

1062 respective conformation.

1063

1064 **Table 1. Cryo-EM data collection, refinement and validation statistics.**

	nhTMEM16, DDM, +Ca^{2+} (EMDB-4588, PDB 6QM5)	nhTMEM16, DDM, -Ca^{2+} (EMDB-4589, PDB 6QM6)	nhTMEM16, 2N2, -Ca^{2+} (EMDB-4587, PDB 6QM4)
Data collection and processing			
Microscope	FEI Talos Arctica	FEI Talos Arctica	FEI Talos Arctica
Camera	Gatan K2 Summit + GIF	Gatan K2 Summit + GIF	Gatan K2 Summit + GIF
Magnification	49,407	49,407	49,407
Voltage (kV)	200	200	200
Exposure time frame/total (s)	0.15/9	0.15/9	0.15/9
Number of frames per image	60	60	60
Electron exposure (e–/Å^2)	52	52	52
Defocus range (μm)	-0.5 to -2.0	-0.5 to -2.0	-0.5 to -2.0
Pixel size (Å)	1.012	1.012	1.012
Box size (pixels)	220	240	240
Symmetry imposed	C2	C2	C2
Initial particle images (no.)	251,693	570,203	1,379,187
Final particle images (no.)	120,086	238,070	133,961
Map resolution (Å)			
0.143 FSC threshold	3.64	3.68	3.79
Map resolution range (Å)	3.4-5.0	3.4-5.0	3.3-5.0
Refinement			
Initial model used	PDB 4WIS	6QM5	6QMB
Model resolution (Å)	3.6	3.7	3.8
FSC threshold			
Model resolution range (Å)	80-3.6	80-3.7	80-3.8
Map sharpening *B* factor (Å^2)	-126	-147	-150
Model composition			
Nonhydrogen atoms	10874	10852	10578
Protein residues	1346	1344	1308
Ligands	4	-	-
B factors (Å^2)			
Protein	55.75	76.42	94.09
Ligand	33.72	-	-
R.m.s. deviations			
Bond lengths (Å)	0.007	0.004	0.007
Bond angles (°)	0.821	0.835	0.983
Validation			
MolProbity score	1.47	1.42	1.53
Clashscore	4.02	4.35	4.09
Poor rotamers (%)	0	0	0
Ramachandran plot			
Favored (%)	95.92	96.74	95.17
Allowed (%)	4.08	3.26	4.83
Disallowed (%)	0	0	0

1065

1066 **Table 2. Cryo-EM data collection, refinement and validation statistics of the Ca^{2+} bound**

1067 **nhTMEM16 in nanodiscs.**

	nhTMEM16, 2N2, +Ca^{2+} open (EMDB-4592, PDB 6QM9)	nhTMEM16, 2N2, +Ca^{2+} intermediate-closed (EMDB-4593, PDB 6QMA)	nhTMEM16, 2N2, +Ca^{2+} closed (EMDB-4594, PDB 6QMB)
Data collection and processing			
Microscope		FEI Talos Arctica	
Camera		Gatan K2 Summit + GIF	
Magnification		49,407	
Voltage (kV)		200	
Exposure time frame/total (s)		0.15/9	
Number of frames per image		60	
Electron exposure (e–/Å^2)		52	
Defocus range (μm)		-0.5 to -2.0	
Pixel size (Å)		1.012	
Box size (pixels)		240	
Symmetry imposed		C2	
Initial particle images (no.)		2,440,110	
Final particle images (no.)	71,175	33,310	41,631
Map resolution (Å)			
0.143 FSC threshold	3.57	3.68	3.57
Map resolution range (Å)	3.4 – 5	3.6 – 5	3.4 – 5
Refinement			
Initial model used	6QM5	6QMB	6QM5
Model resolution (Å)	3.6	3.7	3.6
FSC threshold			
Model resolution range (Å)			
Map sharpening *B* factor (Å^2)	-114	-96	-95
Model composition			
Nonhydrogen atoms	10878	10714	10696
Protein residues	1346	1324	1322
Ligands	4	4	4
B factors (Å^2)			
Protein	77.93	84.86	88.53
Ligand	54.34	57.57	67.10
R.m.s. deviations			
Bond lengths (Å)	0.005	0.006	0.008
Bond angles (°)	0.880	0.872	0.858
Validation			
MolProbity score	1.36	1.38	1.42
Clashscore	3.74	4.69	3.90
Poor rotamers (%)	0	0.18	0
Ramachandran plot			
Favored (%)	96.82	97.23	96.38
Allowed (%)	3.18	2.77	3.62
Disallowed (%)	0	0	0

1068 **Video 1. Conformational transitions.** Shown is a morph between distinct conformational states
1069 obtained for nhTMEM16, namely: the Ca^{2+}-bound 'open' state obtained for nhTMEM16 in
1070 nanodiscs; the 'intermediate' state obtained for nhTMEM16 in lipid nanodiscs; the 'closed' state
1071 obtained for nhTMEM16 in lipid nanodiscs; and the Ca^{2+}-free closed state obtained for
1072 nhTMEM16 in lipid nanodiscs. Shown is a view of the subunit cavity as depicted in Figure 3 and
1073 4. Ca^{2+} ions are shown as blue spheres.

1074 **Video 2. Micelle and lipid distortion.** Shown are the cryo-EM density maps of nhTMEM16
1075 obtained in detergent in complex with Ca^{2+} (upper left corner), in detergent in absence of Ca^{2+}
1076 (upper right corner), in lipid nanodiscs in complex with Ca^{2+} (lower left corner) and in lipid
1077 nanodiscs in absence of Ca^{2+} (lower right corner). The surrounding environment corresponding to
1078 the detergent micelle (upper panels) or the lipid nanodiscs (lower panels) are colored respectively,
1079 while the rest of the protein is shown in grey. Refined and unmasked cryo-EM maps were low-
1080 pass filtered to 6 Å. Transmembrane α-helices 4 and 6 are labeled at the end, indicating the position
1081 of the subunit cavity.